THESIS FOR THE DEGREE OF DOCTOR OF PHILOSOPHY

Significance of grain boundaries for transport phenomena in graphene and proton-conducting barium zirconate

EDIT HELGEE

Department of Applied Physics
CHALMERS UNIVERSITY OF TECHNOLOGY
Göteborg, Sweden 2015

Cover: Proton concentration near a barium zirconate grain boundary (top left), a barium zirconate grain boundary (bottom left), buckling of graphene grain boundary (top right) and structure of graphene grain boundary (bottom right)

Typeset in LATEX. Figures created using Matlab, ASE, VMD, VESTA and Inkscape.

Significance of grain boundaries for transport phenomena in graphene and proton-conducting barium zirconate
EDIT HELGEE

Department of Applied Physics
Chalmers University of Technology

ABSTRACT

Grain boundaries can have a significant influence on the properties of polycrystalline materials. When determining the type and extent of this influence it is frequently useful to employ computational methods such as density functional theory and molecular dynamics, which can provide models of the grain boundary structure at the atomistic level. This work investigates the influence of grain boundaries in two different materials, barium zirconate and graphene, using atomistic simulations.

Barium zirconate is a proton conducting material with a potential application as a fuel cell electrolyte. However, the presence of grain boundaries has been found to lower the proton conductivity. Here, density functional theory has been used to investigate the segregation of positively charged defects, such as oxygen vacancies and protons, to the grain boundaries. It has been found that both defect types segregate strongly to the grain boundaries, which gives rise to an electrostatic potential that depletes the surrounding region of protons and impedes transport across the grain boundary. A thermodynamical space-charge model has been employed to relate the theoretical results to experimentally measurable quantities.

The carbon allotrope graphene has many potential applications in for example electronics, sensors and catalysis. It has also been mentioned as a possible material for phononics and heat management applications due to its unique vibrational properties, which give it a high thermal conductivity. Grain boundaries have been found to decrease the thermal conductivity, but they may also provide a method for manipulating the vibrational properties. The work included in this thesis investigates the scattering of long-wavelength flexural phonons, i.e. phonons with polarization vectors pointing out of the graphene plane, at grain boundaries. Grain boundaries in graphene frequently cause out-of-plane deformation, buckling, of the graphene sheet, and it is found that this buckling is the main cause of scattering of long-wavelength flexural phonons. Based on this result a continuum mechanical model of the scattering has been constructed, with a view to facilitating the study of systems too large to be modelled by molecular dynamics.

LIST OF PUBLICATIONS

This thesis consists of an introductory text and the following papers:

I Oxygen vacancy segregation and space-charge effects in grain boundaries of dry and hydrated BaZrO$_3$
B. Joakim Nyman, Edit E. Helgee and Göran Wahnström
Applied Physics Letters **100** 061903 (2012)

II Oxygen vacancy segregation in grain boundaries of BaZrO$_3$ using interatomic potentials
Anders Lindman, Edit E. Helgee, B. Joakim Nyman and Göran Wahnström
Solid State Ionics **230** 27 (2013)

III Origin of space charge in grain boundaries of proton-conducting BaZrO$_3$
Edit E. Helgee, Anders Lindman and Göran Wahnström
Fuel Cells **13** 19 (2013)

IV Scattering of flexural acoustic phonons at grain boundaries in graphene
Edit E. Helgee and Andreas Isacsson
Physical Review B **90** 045416 (2014)

V Diffraction and near-zero transmission of flexural phonons at graphene grain boundaries
Edit E. Helgee and Andreas Isacsson
(Submitted to Physical Review B)

Specification of the author's contribution to the publications

I The author prepared the atomic configurations for simulations and contributed to analyzing the results, and assisted in writing the paper.

II The author conducted preparatory simulations with the interatomic potential, contributed to the thermodynamical modelling and assisted in writing the paper.

III The author did the thermodynamical modelling and most of the density functional theory calculations, and wrote the paper.

IV The author conducted all molecular dynamics and continuum mechanical simulations, and wrote the paper.

V The author conducted all molecular dynamics and continuum mechanical simulations, and wrote the paper.

Not included in this thesis are the following publications

I Theoretical modeling of defect segregation and space-charge formation in the BaZrO$_3$ (210)[001] tilt grain boundary
Anders Lindman, Edit E. Helgee and Göran Wahnström
Solid State Ionics **252** 121 (2013)

II Adsorption of metal atoms at a buckled graphene grain boundary using model potentials
Edit E. Helgee and Andreas Isacsson
(Manuscript)
http://publications.lib.chalmers.se/records/fulltext/
214089/local_214089.pdf

Contents

Chapter 1

Introduction

Many materials in the world around us derive some of their properties from the defects they contain. The presence of defects can make a material less useful, but can also open the possibility of tuning its properties. For instance, the electronic conductivity of semiconductors can be manipulated through introduction of point defects, also known as dopants, a process that is fundamental to the semiconductor industry [1]. Line defects or dislocations are important for the mechanical properties of metals, and two-dimensional defects such as grain boundaries can change both the mechanical, chemical and electronic properties of a material [1–3]. This thesis describes the influence of grain boundaries in two materials, barium zirconate and graphene.

1.1   What are grain boundaries?

In a crystalline material, a unit cell consisting of one or several atoms is repeated in all directions, resulting in a periodic structure. A sample of a crystalline material can be either a single crystal, if the periodic structure is unbroken throughout, or polycrystalline, if it consists of several smaller single crystal grains with different orientations. In a polycrystalline sample, the interface between two grains with the same composition and structure but different orientations is a grain boundary (see Figure 1.1).

Since the perfect crystal structure is usually the configuration with lowest energy, it may seem strange that grain boundaries should form at all. That they do occur is typically a consequence of how the sample was produced. As an example, consider solidification of a molten substance. For temperatures slightly below the melting point, solid particles will begin to form at several points in the melt. As the temperature drops, the solid particles will grow larger until the surfaces meet. In most cases the particles do not have the same orientation, leading to a mismatch between the crystal lattices. Theoretically, the grains could be rotated to the same orientation, but in practice this would require too much energy. Instead, a grain boundary is formed as a metastable state [1–3].

Although grain boundaries typically occur as a result of adjacent grains growing
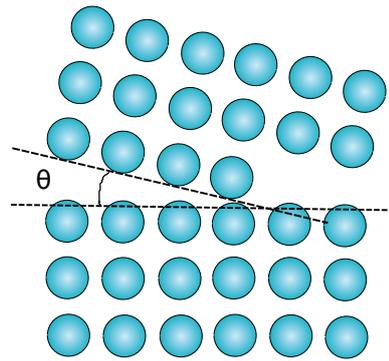
Figure 1.1: Two grains with the same structure and composition, but rotated by an angle θ with respect to each other, forming a grain boundary.

(a)   (b)
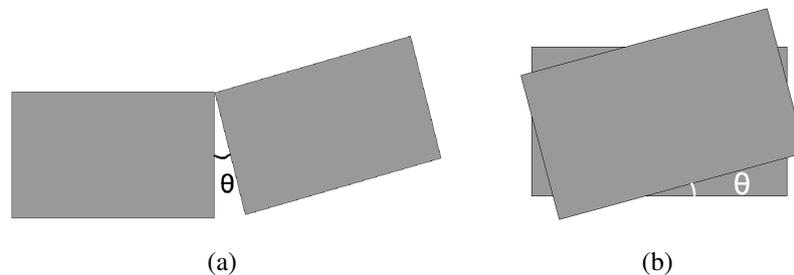
Figure 1.2: Schematic depicting the construction of a tilt grain boundary (a) and a twist grain boundary (b) with misorientation angle θ.

together, it is more convenient to build theoretical descriptions on the differences between the grain boundary and bulk, as well as on the relative displacement of the grains. To create a grain boundary in a single crystal slab, one first has to divide the sample into two parts along some direction. A lattice mismatch can then be created by rotating the two parts relative to each other by some angle, or by displacing one part with respect to the other along or perpendicular to the interface. Putting the two parts together again, one will have obtained a grain boundary that can be classified according to the misorientation angle, the crystal plane along which the slab has been cut, and the relative displacement of the grains [1]. If the axis of rotation is perpendicular to the interface the result is a twist grain boundary, as opposed to a tilt grain boundary where the axis of rotation is parallel to the interface (see Figure 1.2). The grains may be also rotated around two axes, one parallel and one perpendicular to the boundary plane, resulting in a grain boundary that is a combination of tilt and twist. This is often the case for real grain boundaries. The creation of a grain boundary is associated with a grain boundary energy γ with units of energy per area.

Due to the lattice mismatch between the grains, the grain boundary will frequently contain both voids and regions with atom-atom distances shorter than those in bulk. This introduces a strain in the lattice, thereby causing distortions in the re-

gion close to the grain boundary. The altered structure at and near the grain boundary will naturally affect the local vibrational and electronic properties, and may also reduce the strength of the material [1, 3]. In addition, point defects such as vacancies, interstitials and impurities frequently have a different energy of formation at the grain boundary, leading to segregation of defects [2]. This could for example affect the mechanical strength. If the segregated defects are charged, as may be the case in semiconductors and ionic systems, segregation can also lead to the boundary aquiring a net charge.

1.2   Thesis outline

In this thesis, the effect of grain boundaries on transport properties in two different materials is investigated using atomistic simulations. The first material is yttrium-doped barium zirconate, a proton-conducting oxide with a potential application as an electrolyte in solid oxide fuel cells. The grain boundaries of barium zirconate have been shown to substantially impede proton transport. Here, the segregation of oxygen vacancies and protons to barium zirconate grain boundaries is studied in order to ascertain whether they could cause the grain boundary to obtain a positive net charge, depleting the surrounding region of protons and thereby lowering the proton conductivity.

The second material studied is graphene, a carbon sheet of single atom thickness. Although grain boundaries in graphene have been shown to affect both electronic and mechanical properties, the focus here is on phonon transport. Specifically, we have studied the scattering of long-wavelength out-of-plane acoustic phonons, which are important for *e.g* heat transport.

The thesis will be organized as follows: Chapter 2 introduces the potential application of barium zirconate in fuel cells, and gives an overview of the defect chemistry of the material. Chapter 3 descibes phonon transport in graphene, and also how grain boundaries in a two-dimensional material like graphene differ from those in an ordinary material. Chapter 4 gives an overview of the computational methods used and Chapters 5 and 6 provide a summary of the results, conclusions and outlook concering barium zirconate and graphene, respectively.

Chapter 2

Proton-conducting BaZrO$_3$

Barium zirconate, BaZrO$_3$, has been studied extensively during the last three decades. The main reason is that doped barium zirconate is a proton conductor, and it may therefore be useful for electrolysis of water and as an electrolyte material in fuel cells. A fuel cell is a device that transforms the chemical energy stored in fuel into useful work, similarly to the ubiquitous internal combustion engine. However, while in the internal combustion engine the heat generated by burning fuel causes a gas to expand, thereby generating work, the fuel cell converts chemical energy directly into electrical energy. This gives the fuel cell a higher efficiency compared to the internal combustion engine [4, 5].

In addition to their higher efficiency, fuel cells may also be a key to replacing fossil fuels with renewable alternatives due to their ability to run on pure hydrogen. In the ideal scenario, known as the hydrogen economy, hydrogen could be sustainably produced from *e.g.* solar-powered photocatalytic reactions or biological processes, and then used to power fuel cells in for example cars and other vehicles [6, 7]. This process would result in near-zero emission of greenhouse gases and eliminate the need for fossil fuels. However, sustainable hydrogen production and storage are technologically challenging, and fuel cell technology must also be developed further before the hydrogen economy can be realized.

In the first part of this chapter, a brief overview of the basic principles of fuel cells is given and the requirements that an electrolyte material must meet are discussed. The second part of the chapter gives a more thorough introduction to the defect chemistry of barium zirconate and describes how the influence of grain boundaries may be explained.

2.1   Fuel cells

2.1.1   Basic principles

To extract electrical energy directly from a combustion process, the reaction must be split into an oxidation part and a reduction part. As an example, consider the combustion of hydrogen. When hydrogen gas is ignited in the presence of oxygen,

water is produced according to the following reaction:

$$H_2 + \frac{1}{2}O_2 \rightarrow H_2O \tag{2.1}$$

This reaction is exothermic and will release energy in the form of heat. If the hydrogen is instead used as fuel in a fuel cell, oxygen and hydrogen are supplied at different locations in the cell (see Figure 2.1). At the anode, hydrogen gas is split and incorporated into the electrode material according to the oxidation reaction

$$H_2 \rightarrow 2H^+ + 2e^-. \tag{2.2}$$

The free electrons generated in this process flow through an electrical circuit, where work is extracted, to get to the cathode. At the cathode, oxygen gas undergoes reduction and forms ions:

$$\frac{1}{2}O_2 + 2e^- \rightarrow O^{2-}. \tag{2.3}$$

Finally, the products of the previous reactions combine to form water:

$$2H^+ + O^{2-} \rightarrow H_2O. \tag{2.4}$$

The water formation step may take place either at the cathode or at the anode depending on the properties of the electrolyte. A proton-conducting electrolyte enables the protons to travel through the cell, forming water with the oxygen ions at the cathode. If the electrolyte is an oxygen ion conductor, the oxygen ions will instead travel to the anode and water will form there [4, 5].

In order for the fuel cell to function efficiently, the reactions must proceed at a high speed and be kept separated. This means that the component materials must have a specific set of properties. The electrodes should be efficient catalysts for the splitting reactions (Equations 2.2 and 2.3), and also be good electronic conductors so that electrons can be transported to and from the electric load. Ideally, the electrodes should also be ionic conductors so that ions can be transported through the electrode to the electrolyte. This enables the splitting reaction to take place anywhere on the electrode surface. If the electrode is not an ionic conductor, the reaction is restricted to points where the electrode, electrolyte and gas are in contact. The electrolyte should have a high ionic conductivity, but must also be impermeable to gas molecules and electrically insulating, as electrons passing through the electrolyte would short-circuit the cell. Finally, the component materials must be chemically stable under fuel cell operating conditions. This means that they must not react with each other at the operating temperature of the cell, and they must also be stable in the presence of water and carbon oxides [5, 8].

2.1.2 Types of fuel cells

Efficient fuel cell operation can be accomplished using a number of different combinations of electrode and electrolyte materials. As a consequence there are several
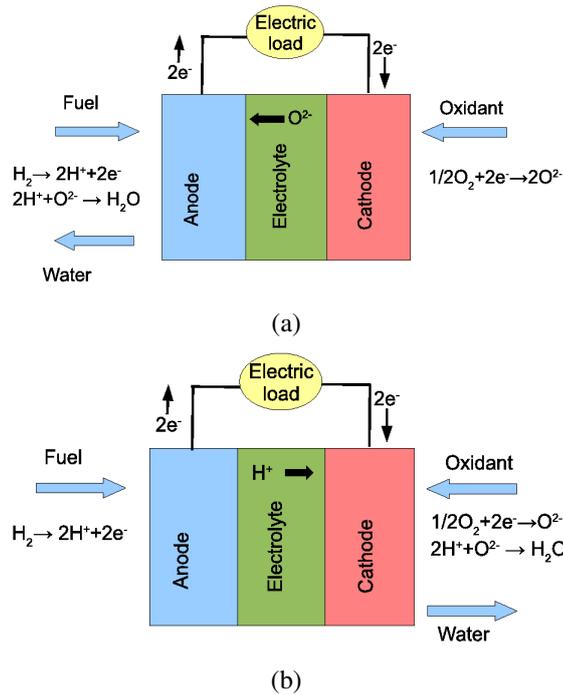
Figure 2.1: Schematic of fuel cells with (a) an oxygen ion conducting electrolyte and (b) a proton conducting electrolyte.

types of fuel cells, each with their own advantages and drawbacks. Most existing fuel cell types belong to one of two categories: Low-temperature fuel cells, with operation temperatures below 200 °C, or high-tempterature fuel cells with operation temperatures between 700 and 1000 °C. An exception is molten carbonate fuel cells, with operation temperatures between 500 and 700 °C. The operation temperature is mainly determined by the temperature interval in which the electrolyte is an efficient enough ionic conductor [5, 8].

In low-temperature fuel cells, typical electrolytes are solid polymer membranes, liquid solutions of alkaline salts, and phosphoric acid. Solid polymer membranes like Nafion require operation temperatures between 70 and 100 °C, while alkaline solutions and phosphoric acid cells can be used at temperatures between 100 and 250 °C [8]. The low operation temperatures of these fuel cells give them short startup times and make them suitable for mobile applications, such as replacing internal combustion engines and batteries. However, in this temperature range noble metal catalysts, usually platinum, are required for the hydrogen splitting reaction. This makes the fuel cells more expensive and renders them sensitive to carbon in the fuel, as carbon oxides bind very strongly to platinum and thus block reaction sites for the splitting reaction (catalyst poisoning). Only pure hydrogen can therefore be used as fuel, except in direct-methanol fuel cells where alloys of platinum and other metals, often ruthenium, are used to enable the use of a hydrocarbon fuel. The alkaline and phosphoric acid cells have the additional drawback that the liquid

7

electrolyte might leak out if the cell is damaged. This is especially problematic as both liquids are corrosive [5].

High-temperature fuel cells contain solid oxide electrolytes such as yttrium-stabilized zirconium oxide or doped cerium oxide [9], which function at temperatures between 700 and 1000 °C. At these temperatures, hydrocarbons can be reformed into hydrogen in the fuel cell, and no expensive catalysts are needed. This increased fuel flexibility can be a great advantage. On the other hand, a high operation temperature increases the startup time, as well as requiring the cell to be thermally isolated from its surroundings. This makes high-temperature fuel cells less useful for mobile applications. The high temperature also increases the risk of reactions or interdiffusion between the cell components, and differences between the thermal expansion coefficients of the components can lead to the formation of cracks in the cell during heating or cooling [8].

Considering the advantages and drawbacks of high- and low-temperature fuel cells, it becomes clear that a fuel cell with operation temperature in the intermediate range, 200 to 700 °C, could have several very attractive features. It might for instance have the same fuel flexibility as a high-temperature fuel cell, but without the high risk of interdiffusion and crack formation. However, the only existing fuel cells operating in this temperature range are molten carbonate fuel cells, which have a number of drawbacks. For instance, the molten carbonate electrolyte is a liquid and may therefore leak out of the fuel cell. It can be destroyed by repeated solidification and melting, requiring it to be kept above its melting temperature also when the cell is not in use. Similarly to the low-temperature liquid electrolytes it is corrosive [8].

What appears to be needed is thus a solid electrolyte with operation temperature between 200 and 700 °C. To function as an efficient electrolyte, the material must have a high ionic conductivity in this temperature range, as well as being an electronic insulator. As will be shown in the next section, barium zirconate may meet these criteria.

2.2   Properties of BaZrO$_3$

Barium zirconate belongs to a group of oxides called perovskites. The composition of an undoped perovskite follows the formula ABX$_3$, where A and B are cations and X usually stands for oxygen ions. The A cation is often bivalent (charge $+2e$) and the B cation tetravalent ($+4e$), as is the case in barium zirconate. Barium zirconate is normally found in the cubic perovskite structure shown in Figure 2.2, but other perovskites may appear in an orthorombic or tetragonal version of this structure.

Proton conductivity in doped perovskite oxides was first discovered in the 1980:s by Iwahara and coworkers [10–12]. The first studies consider barium and strontium cerates, but later on calcium, strontium and barium zirconate were also found to conduct protons when doped and exposed to water vapour [13]. It was found that the activation energy for proton transport in these oxides is generally lower than the activation energy for oxygen ion transport in conventional solid oxide ionic con-
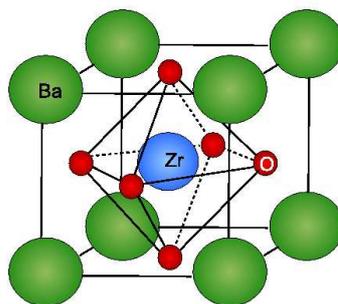
Figure 2.2: The cubic perovskite structure of BaZrO$_3$.

ductors, which gives the proton-conducting perovskites a higher conductivity in the intermediate-temperature range (see Figure 2.3). Later studies have found similar proton conductivity also in oxides with other structures [9, 14].

Among the proton-conducting oxides, doped barium zirconate stands out as a particularly interesting electrolyte material since it is an electronic insulator and chemically stable under fuel cell operating conditions. However, the total proton conductivity is lower than that of, for example, the less chemically stable oxide barium cerate. Experimental measurements have shown that the total proton conductivity of barium zirconate must be divided into a grain interior component and a grain boundary component. The grain interior conductivity is high, comparable to that of other oxides, while the proton conductivity of the grain boundaries is much lower and significantly reduces the total conductivity [16–18] (Figure 2.4). The grain boundary conductivity remains low even when the grain boundaries are free of segregated impurity phases [19–21], in contrast to for example zirconium oxide where blocking layers of amorphous material impede transport across grain boundaries [22].

The high resistivity of grain boundaries in barium zirconate is especially problematic due to the poor sinterability of the material, which leads to small grains and thus a high number of grain boundaries. In the search for ways to reduce the resistivity of barium zirconate, attempts have been made to improve sinterability by making solid solutions with barium cerate, co-doping with *e.g.* strontium or indium, employing sintering aids such as zinc oxide [14, 25], or optimizing fabrication techniques [26, 27]. While co-doping with strontium or indium has been shown to produce high conductivity [28, 29], theoretical studies suggest that using zinc oxides as sintering aids may reduce the proton mobility due to a strong attraction between the proton and the zinc ion [30, 31]. Attempts are also being made to use thin films, which can be produced as single crystals [14, 25, 32].

Other efforts have been focused on finding the cause of the low grain boundary conductivity. While it has been suggested that structural effects such as the lattice distortion at the boundary may be of relevance [16, 33], most studies have focused on the space-charge effect that is known from grain boundaries in other oxides. In *e.g.* yttria-stabilized zirconia, doped ceria and strontium titanate, some of the effects of

9
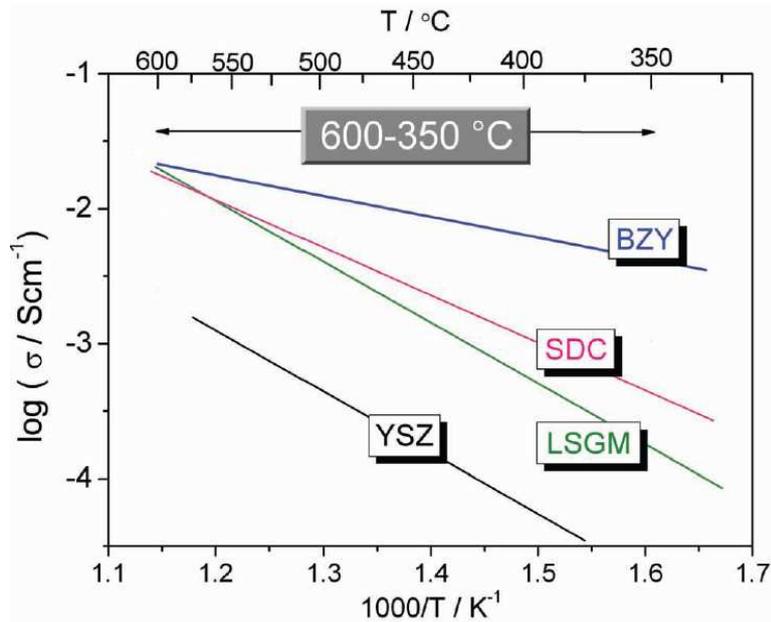
Figure 2.3: Temperature dependence of the conductivity of the oxygen ion conductors yttria-stabilized zirconia (YSZ), Sm-doped ceria (SDC) and doped lanthanum gallate (LSGM) compared to the proton conductor yttrium-doped barium zirconate (BZY). Figure from Ref. [15], ©2012 WILEY-VCH Verlag GmbH & Co. KGaA, Weinheim, reprinted with permission.
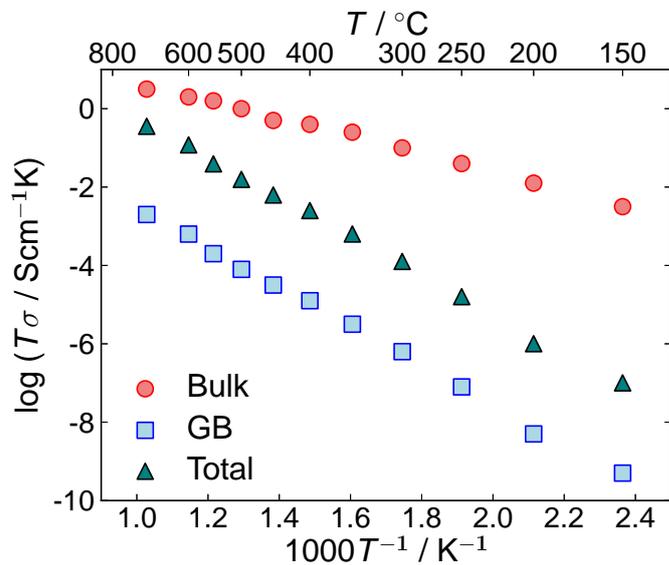
Figure 2.4: Comparison of bulk, grain boundary and total conductivity in BaZrO$_3$. Bulk and grain boundary conductivities are taken from Ref. [23]. The total conductivity is calculated assuming a grain size of 1 μm. Figure from [24], reprinted with permission.
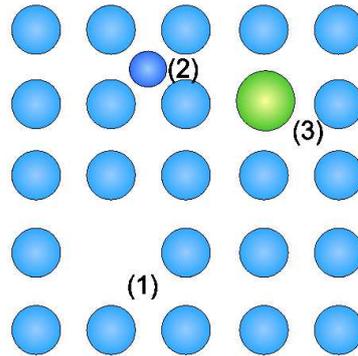
Figure 2.5: Schematic depicting point defect types, a vacancy (1), an interstitial (2) and a substitutional defect (3).

grain boundaries on conductivity can be explained by charged defects aggregating at the grain boundary and giving it a net charge [34, 35]. This leads to the surrounding volume, termed the space charge layers, being depleted of mobile charged defects of the same polarity as the boundary charge. Experimental studies have suggested that this model may also be applicable to barium zirconate [20, 23, 36–40], indicating the existence of a positive grain boundary charge that depletes the surrounding material of protons.

2.3 Point defects in BaZrO$_3$

In its pure form, barium zirconate does not contain any protons and is not a very good ionic conductor. To turn it into a proton conductor, it has to be doped and exposed to water vapour. This section describes how doping, *i.e.* the intentional introduction of point defects, leads to the incorporation of protons and how the protons move through the material.

Point defects are present in all real materials at finite temperature due to the significant increase in entropy caused by introducing a point defect into a perfect lattice. In general, there are three types of point defects: Vacancies, substitutional defects, and interstitials. A vacancy is formed when an atom is taken out of the material, leaving the lattice site empty. If the atom is instead replaced by an atom of a different species, a substitutional defect is formed. Interstitials, finally, occupy positions between the atoms of the regular lattice. A schematic illustration can be seen in Figure 2.5.

In barium zirconate, additional point defects are introduced in order to make the material a proton conductor. This is done by replacing some of the tetravalent zirconium ions with trivalent metal ions. To understand the effects of this substitution, it is perhaps easiest to begin by imagining the atomic constituents of one unit cell of pure barium zirconate, *i.e.* one barium atom, one zirconium atom and three oxygen

atoms. When the five atoms combine to form barium zirconate, the barium atom will donate two electrons and thus become an ion with a charge of $+2$ in units of the elementary charge. The zirconium atom will donate four electrons and the ion will have the charge $+4$, while the oxygen atoms will receive two electrons each and form ions with charge -2. Together, the ions form a charge neutral, stable material.

If the zirconium atom is replaced by a metal atom that can only donate three electrons, one of the oxygen ions will be missing an electron. As in semiconductors, the missing electron can be thought of as an electron hole. Also in analogy to semiconductors, trivalent dopants at the zirconium site in barium zirconate are termed acceptor dopants since they cause formation of an electron hole. However, there is also another possibility: two electron holes together with one oxygen ion could make a neutral oxygen atom, which then leaves the material and thus generates an oxygen vacancy. Whether this happens or not depends on the oxygen partial pressure in the surrounding atmosphere. For barium zirconate, it has been shown that oxygen vacancies occur in larger amounts than electron holes except at very high oxygen partial pressures [41].

Doped barium zirconate will thus contain dopant atoms, which are substitutional defects, and oxygen vacancies. Both defect types will have a different charge compared to the ion occupying the same place in the undoped material. For example, the dopant ion has the charge $+3$ and is replacing a zirconium ion with the charge $+4$. Compared to the undoped material, the dopant thus has an effective charge of $3 - 4 = -1$. In the same way, the vacancy is replacing an oxygen ion with the charge -2 and therefore has the effective charge $+2$. This can be expressed using the Kröger-Vink notation for defects. According to this notation, an yttrium dopant is written Y'_{Zr}, where Y is the chemical symbol for yttrium, the subscript "Zr" signifies that it occupies a zirconium site and the single aphostrophe indicates the effective charge -1. Correspondingly, the vacancy is denoted by $V_O^{\bullet\bullet}$, where the "V" stands for vacancy, the "O" shows that it occupies the oxygen site and the two dots give the effective charge as $+2$. Interstitial defect sites are denoted by the letter "I", so that an interstitial tetravalent zirconium ion would be written as $Zr_I^{\bullet\bullet\bullet\bullet}$ [2].

Finally, the protons are introduced by exposing the doped barium zirconate to water vapour. The oxygen vacancies are then filled with hydroxide ions according to the hydration reaction

$$H_2O(g) + V_O^{\bullet\bullet} + O_O^\times \rightleftharpoons 2OH_O^\bullet, \tag{2.5}$$

where $O_O^\times$ is an effectively neutral oxygen ion at an oxygen site. Protons will thus be present in the material as part of effectively positive hydroxide ions, $OH_O^\bullet$. The proton conductivity will depend on the proton diffusion coefficient, which will be discussed in section 2.3.2, and on the concentration of hydroxide ions. The concentration in turn depends on the temperature and the partial pressure of water vapour. To determine the equilibrium concentrations of hydroxide ions and oxygen vacancies at a given temperature and partial pressure, the change in Gibbs' free energy associated with the hydration reaction must be considered.

2.3.1 Defect equilibrium

To obtain an expression for the defect concentrations, we start by deriving the relation between defect concentration and a change in Gibbs' free energy for a general case. Consider a model material, consisting of a single element denoted M. A vacancy can be formed by removing an atom from the middle of the lattice and placing it on the surface:

$$M_M \rightleftharpoons M_{surf} + V_M. \tag{2.6}$$
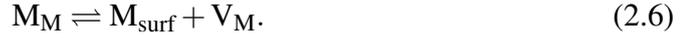
Here, M_S denotes an atom of element M on a surface (surf) site. This reaction will be associated with an enthalpy of formation ΔH^f and an entropy of formation ΔS^f. The enthalpy of formation has two main contributions, one being the change in energy resulting from breaking the bonds in the lattice and forming bonds at the surface. The other contribution is the energy and volume change that arises as the atoms near the vacancy are displaced from their equilibrium positions in a way that minimizes the energy cost of the vacancy. The entropy of formation is due to the changes in lattice vibrations caused by the introduction of the vacancy [2].

In addition to these two quantities, there is also a change in the configurational entropy of the system. Unlike the entropy of formation, which depends on the specific material, the configurational entropy change ΔS^{conf} can be calculated from a general expression provided that the defect concentration is low and the defects do not interact. Suppose that N_D defects have been formed in a lattice containing N sites in total. The number of possible ways to arrange these defects on the lattice is

$$\Omega = \binom{N}{N_D} = \frac{N!}{N_D!(N-N_D)!}, \tag{2.7}$$

which gives the configurational entropy

$$\Delta S^{conf} = k_B \ln \Omega = k_B \ln \frac{N!}{N_D!(N-N_D)!}. \tag{2.8}$$

Assuming that N and N_D are very large numbers, we can use Stirling's approximation to obtain

$$\Delta S^{conf} \approx k_B \left(N \ln \frac{N}{N-N_D} - N_D \ln \frac{N_D}{N-N_D} \right). \tag{2.9}$$

Since we have assumed that the defects do not interact, we can write the total Gibbs' free energy of a system with N_D defects as

$$G = G^{pure} + \Delta G = G^{pure} + N_D \Delta H^f - N_D T \Delta S^f - T \Delta S^{conf}, \tag{2.10}$$

where G^{pure} is the Gibbs' free energy of the lattice without defects. We can then obtain the chemical potential of the defect by differentiating with respect to the number of defects [2]:

$$\mu_D = \left(\frac{\partial G}{\partial N_D} \right)_{T,P} = \Delta H^f - T \Delta S^f + k_B T \ln \frac{N_D}{N-N_D}. \tag{2.11}$$

The ratio of the number of defects to the total number of sites, N_D/N gives the defect concentration c_D. Denoting the maximum defect concentration with c_0 and inserting this into the above equation yields

$$\mu_D = \Delta H^f - T\Delta S^f + k_B T \ln \frac{c_D}{c_0 - c_D}. \tag{2.12}$$

If the defect concentration is very low we can approximate the denominator in the logarithm with c_0 and obtain

$$\mu_D = \Delta H^f - T\Delta S^f + k_B T \ln \frac{c_D}{c_0}. \tag{2.13}$$

This is known as the dilute approximation. In equilibrium, the Gibbs' free energy is at a minimum with respect to changes in the defect concentration. This means that the chemical potential must be zero, which gives

$$c_D = c_0 \exp\left(-\frac{\Delta H^f - T\Delta S^f}{k_B T}\right). \tag{2.14}$$

Equation 2.14 describes the relation between the Gibbs' free energy of formation and the defect concentration for a single defect type, but the hydration of barium zirconate involves two defect species in equilibrium with a surrounding atmosphere. In a general chemical reaction with two reactants and two products, where a moles of species A and b moles of species B form c and d moles of species C and D,

$$a\text{A} + b\text{B} \rightleftharpoons c\text{C} + d\text{D}, \tag{2.15}$$

the change in Gibbs' free energy of the system can be obtained as the free energy of the products minus the free energy of the reactants,

$$\Delta G = c\mu_C + d\mu_D - (a\mu_A + b\mu_B). \tag{2.16}$$

The chemical potential of reactant i is given by

$$\mu_i = \mu_i^\circ + k_B T \ln a_i \tag{2.17}$$

where a_i is the activity and μ_i° is known as the standard chemical potential. Comparing to Equation 2.13, we see that for a defect in the dilute limit we have $a_i = c_i$ and $\mu_i^\circ = \Delta H^f - T\Delta S^f$. Setting $\Delta G^\circ = c\mu_C^\circ + d\mu_D^\circ - a\mu_A^\circ - b\mu_B^\circ$, we find the *law of mass action*:

$$\frac{c_C^c c_D^d}{c_A^a c_B^b} = \exp\left(-\frac{\Delta G^\circ}{k_B T}\right) \equiv K, \tag{2.18}$$

For reactants in the gas phase the activity is taken to be equivalent to the partial pressure of the gas. The constant K is referred to as the equilibrium constant of the reaction.

Applying the law of mass action to the hydration reaction, Equation 2.5, we obtain

$$K_{\text{hydr}} = \frac{c_{\text{OH}}^2}{c_V c_O p_{\text{H}_2\text{O}}}, \tag{2.19}$$

where p_{H_2O} is the water vapour partial pressure. There are now three species that may occupy the oxygen sites in the lattice: Oxygen ions, oxygen vacancies and hydroxide ions. If we define the concentrations to be measured per unit cell, this gives the site restriction

$$3 = c_O + c_V + c_{OH} \tag{2.20}$$

since each unit cell contains three oxygen sites (*i.e.* $c_0 = 3$). The condition of charge neutrality also gives a relation between the concentrations of vacancies, hydroxide ions and dopants:

$$2c_V + c_{OH} = c_A, \tag{2.21}$$

where c_A is the dopant concentration. Combining these equations and setting $\kappa = p_{H_2O}K_{hydr}$ we get the following expression for the concentration of hydroxide ions

$$c_{OH} = \frac{3\kappa}{\kappa - 4} \left[1 - \sqrt{1 - \frac{\kappa - 4}{3\kappa} c_A \left(2 - \frac{c_A}{3} \right)} \right]. \tag{2.22}$$

Using this expression, it can be seen that the proton concentration depends on the dopant concentration and water partial pressure, and also on temperature through the equilibrium coefficient K_{hydr}. This will in part determine the behaviour of the proton conductvity. To obtain a full expression for the conductivity, however, we must also consider the diffusion coefficient.

2.3.2 Diffusion and conductivity

Before writing down an expression for the diffusion coefficient, we consider the diffusion mechanism. As part of a hydroxide ion, the proton is embedded in the electron cloud of the oxygen ion [42]. The proton can rotate around the host oxygen but also form hydrogen bonds with neighbouring oxygen ions. The hydrogen bond distorts the lattice and brings the oxygens closer to each other [43]. In this configuration it is possible for the proton to jump between the oxygen ions, aided by the lattice distortion (Figure 2.6) [44, 45]. This diffusion mechanism, consisting of alternate rotation and transfer steps, is known as the Grotthus mechanism [16, 42, 46].

As the proton migrates from one oxygen to the next, it crosses two energy barriers. The first barrier is associated with breaking the hydrogen bond to a neighbouring oxygen ion and rotating to form a hydrogen bond with a different neighbouring oxygen ion, and the second barrier is associated with the actual transfer between one oxygen ion and the next. Taken together, these two energy barriers give the activation enthalpy of proton migration, ΔH^{diff}. The activation enthalpy can be influenced by local distortions in the lattice, which may for example occur close to a dopant ion. There is also an entropy change ΔS^{diff} related to the migration process.

In addition to their distorting effect on the nearby lattice, dopant ions may also influence the diffusion of protons due to the electrostatic attraction between the effectively negative dopant and the effectively positive proton, as well as by changing the chemical properties of nearby oxygen ions. These effects frequently lead to
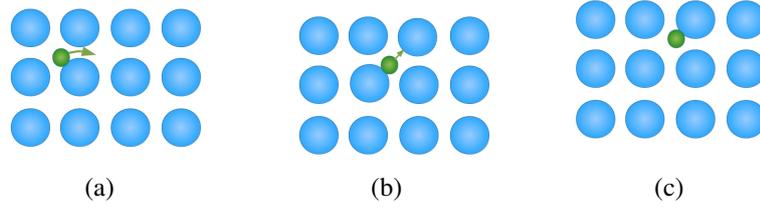
Figure 2.6: Schematic depicting the movement of a proton (green) in the oxygen sublattice (blue). The proton will first rotate around the oxygen ion (a) and then transfer to a second oxygen ion aided by relaxation of the oxygen lattice (b). Figure (c) shows the proton at the second oxygen ion.

trapping of protons close to dopant ions [47–52]. The strength of the trapping inter-action will depend on which metal is used as dopant. For barium zirconate, it has been found that yttrium dopants cause weaker trapping than other dopants and thus have a smaller detrimental effect on the proton conduction [16, 47–51].

To connect the atomistic-level proton diffusion mechanism, the activation en-thalpy, and the experimentally measurable conductivity, we now turn to the dif-fusion coefficient. The diffusion coefficient is proportional to $e^{-\Delta G^{\mathrm{diff}}/k_{\mathrm{B}}T}$, where $\Delta G^{\mathrm{diff}} = \Delta H^{\mathrm{diff}} - T\Delta S^{\mathrm{diff}}$ is the change in Gibb's free energy related to the proton transfer. The diffusion coefficient also depends on the number of nearest-neighbour sites n, the fraction of occupied sites k, the distance between sites a, a correlation factor f and a characteristic frequency ν. The correlation factor accounts for effects of the lattice geometry and the frequency is a measure of how often the proton is in a position to overcome the energy barrier [53, 54]. Together, this gives

$$D(T) = \frac{n}{6}f(1-k)a^2\nu\exp\left(-\frac{\Delta G^{\mathrm{diff}}}{k_{\mathrm{B}}T}\right) \tag{2.23}$$

The conductivity depends on both the diffusion coefficient and the charge num-ber and concentration of the charge carriers, and can be expressed as

$$\sigma = zec\frac{ze}{k_{\mathrm{B}}T}D \tag{2.24}$$

where z is the charge number of the diffusing species, e is the elementary charge and c is the concentration. The factor $zeD/k_{\mathrm{B}}T$ is called the mobility of the defect [45].

2.3.3 Space charge

Finally, we turn to the effects of grain boundaries on the proton conductivity. As previously mentioned, there are two main explanations. According to one theory, the lattice distortion near the boundary alters the distances between oxygen ions in that region, thus making it harder for the protons to transfer from one oxygen ion to the next [16]. The other explanation focuses on the possibility of charged

defects accumulating at the grain boundaries, giving rise to a space-charge effect. While lattice distortion certainly exists and may contribute to the low conductivity, experimental studies have found ample evidence of space-charge effects [20, 23, 36–40].

Due to the structural differences between the grain boundary and the perfect lattice, defects often have different free energies of formation at the grain boundary. If the formation energy is lower and the defects are mobile, they may lower the total free energy of the system by segregating to the grain boundary. According to the space charge model, the accumulation of charged defects in the grain boundary leads to it aquiring a net charge, which generates an electrostatic potential near the grain boundary. For a mobile defect with charge z situated some distance from the grain boundary, the chemical potential is then given by

$$\mu = \mu^\circ + k_\mathrm{B} T \ln \frac{c}{c_0 - c} + ze\phi, \qquad (2.25)$$

where the first two terms are the same as in Equation 2.17, and the third incorporates the effect of the electrostatic potential ϕ.

In equilibrium, the chemical potential of the defect must be the same throughout the material. For simplicity, we will consider a one-dimensional model with the grain boundary situated at $x = 0$. If the chemical potential is to be the same at some position x near the boundary and infinitely far from the boundary, we have

$$\mu^\circ(\infty) + k_\mathrm{B} T \ln \frac{c(\infty)}{c_0 - c(\infty)} + ze\phi(\infty) = \mu^\circ(x) + k_\mathrm{B} T \ln \frac{c(x)}{c_0 - c(x)} + ze\phi(x), \quad (2.26)$$

which may be rewritten as

$$\frac{c(x)}{c(\infty)} = \frac{c_0 \exp\left(-\frac{\Delta\mu^\circ(x) + ze\Delta\phi(x)}{k_\mathrm{B} T}\right)}{c_0 + c(\infty)\left[\exp\left(-\frac{\Delta\mu^\circ(x) + ze\Delta\phi(x)}{k_\mathrm{B} T}\right) - 1\right]}. \qquad (2.27)$$

We see that this expression relates the concentration of defects to the potential difference $\Delta\phi(x) = \phi(x) - \phi(\infty)$ and the difference in standard chemical potential $\Delta\mu^\circ(x) = \mu^\circ(x) - \mu^\circ(\infty)$. However, the electrostatic potential must also depend on the charge density according to Poisson's equation:

$$\frac{\mathrm{d}^2\phi}{\mathrm{d}x^2} = -\frac{\rho(x)}{\varepsilon_0 \varepsilon_r}, \qquad (2.28)$$

where in this case the charge density is given by $\rho(x) = \sum_i z_i c_i(x)$. The sum runs over all charged defect types. Combining equations 2.27 and 2.28 we obtain the Poisson-Boltzmann equation

$$\frac{\mathrm{d}^2\Delta\phi}{\mathrm{d}x^2} = -\frac{1}{\varepsilon_0 \varepsilon_r} \sum_i c_i(\infty) z_i \frac{c_{i0} \exp\left(-\frac{\Delta\mu_i^\circ(x) + z_i e\Delta\phi(x)}{k_\mathrm{B} T}\right)}{c_{i0} + c_i(\infty)\left[\exp\left(-\frac{\Delta\mu_i^\circ(x) + z_i e\Delta\phi(x)}{k_\mathrm{B} T}\right) - 1\right]} \qquad (2.29)$$

17
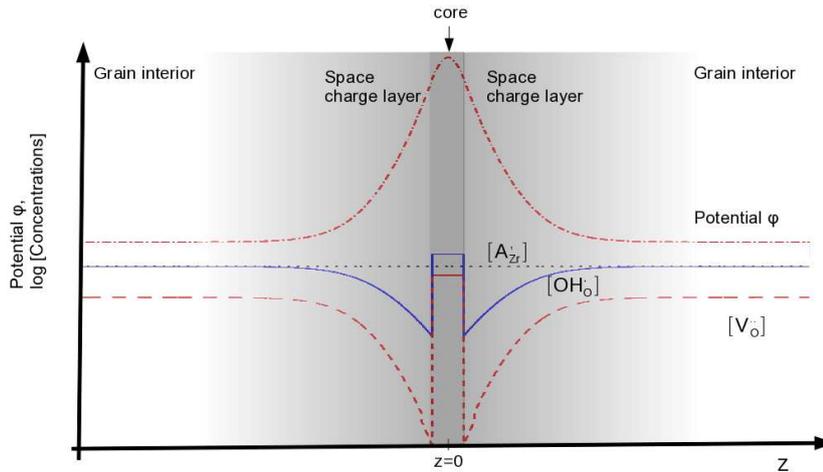
Figure 2.7: Schematic of a grain boundary with space charge layers in BaZrO$_3$, assuming a constant dopant concentration. The figure has been redrawn based on Figure 1 in Paper III.

Using the Poisson-Boltzmann equation it is in theory possible to calculate the concentration of all charged defects close to the boundary, provided that one has access to the difference in standard chemical potential for all defects as a function of *x*. In the space charge model, it is assumed that the difference in standard chemical potential is zero everywhere except very close to the boundary where the lattice is distorted. This region is known as the grain boundary core (Figure 2.7).

Outside of the grain boundary core, the concentrations of mobile defects are determined by the electrostatic potential. This leads to depletion of mobile defects of the same polarity as the boundary core and aggregation of defects with the opposite polarity in the region closest to the core, known as the space charge layers. In the case of barium zirconate, it is thought that the boundary core charge is positive and causes the mobile, effectively positive protons to be depleted. Oxygen vacancies are also mobile at temperatures above 300 K [46], diffusing through a simple hopping mechanism illustrated in Figure 2.8, and would thus be depleted. In contrast, the effectively negative dopant ions have been found to be immobile at temperatures below 1400 K [39], and they are thus unable to migrate to the space-charge layers at lower temperatures. There is, however, evidence that the dopants aggregate in the space charge zones during sintering at high temperature [39, 55].

By using the assumption that the standard chemical potential is only altered in the core and requiring the defect sites in the core to be in equilibrium with the grain interior, it is possible to obtain the barrier height and space charge layer width numerically for different values of $\Delta\mu^\circ$ as a means of investigating the consequences of defect segregation [56]. It is also possible to calculate the difference in formation energy for various defects in the grain boundary compared to the perfect lattice using atomistic simulations. The difference in formation energy, also known as the segregation energy, is thought to be the dominant term in $\Delta\mu^\circ$, and it can therefore
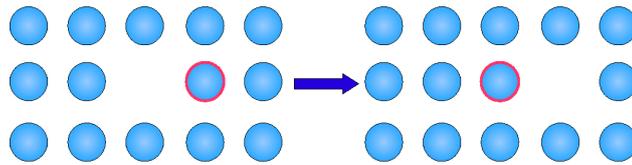
Figure 2.8: Schematic of the vacancy diffusion mechanism. An atom next to the vacancy (picked out in red) moves to fill the vacancy, which is thereby displaced one step to the right.

indicate both if the defects segregate to the boundary at all and if they segregate strongly enough to cause a significant space charge effect. Papers I, II and III report the results of such calculations of the difference in formation energy, as will be further discussed in Chapter 5.

While theoretical studies generate information about segregation energies and concentration profiles, experimental studies typically measure the conductivity. This is done through impedance spectroscopy, a method capable of distinguishing between the grain interior and grain boundary conductivity. Using the relation between conductivity and concentration, the ratio of the grain boundary and bulk conductivities can be used to calculate the average height of the electrostatic barrier at grain boundaries in a polycrystalline sample [20,23,37,38], making it possible to compare experimental and theoretical results.

Chapter 3

Graphene

Unlike barium zirconate, which is mainly studied due to its proton conductivity, graphene has several properties that excite interest. Graphene is an atomically thin layer of graphite, consisting of a single sheet of carbon atoms arranged on a hexagonal lattice. Its unique electron band structure, high strength and low density make graphene both a model system for phenomena involving relativistic electrons and a material with possible practical applications in *e.g.* flexible electronics and sensors [57–60]. It has even been shown that graphene could act as a proton conductor [61].

Many of the special properties of graphene are directly linked to the two-dimensional nature of the material. Of particular importance to this thesis is the impact of the low dimensionality on phonon transport and on the behaviour of grain boundaries. The first part of this chapter therefore gives an introduction to phonons in graphene and how they differ from phonons in ordinary three-dimensional materials. Some of the consequences of these differences are also discussed, in particular with regard to thermal transport. The second part of the chapter describes the properties of grain boundaries in graphene.

3.1 Phonons in graphene

3.1.1 Phonon dispersion

To obtain a qualitative understanding of phonons in three-dimensional materials, picture a crystalline material with a unit cell containing one atom. Each atom in the lattice can move in three dimensions, but due to the interaction with neighbouring atoms there will be a restoring force that brings it back towards its equilibrium position. The exact form of this force is different for different materials, but for small displacements it can be approximated with a harmonic potential.

Let us investigate the consequences of this harmonic approximation for a one-dimensional case, where we also assume that only the nearest neighbours interact. The system can then be represented as a chain of atoms of mass m, at distance a from each other and connected by springs with spring constant C, as illustrated in
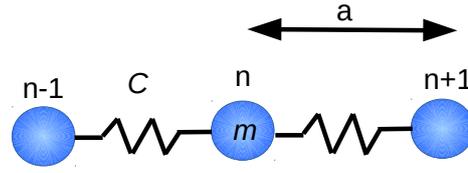
Figure 3.1: A one-dimensional chain of atoms with mass m, at distance a from each other and connected by springs with spring constant C.
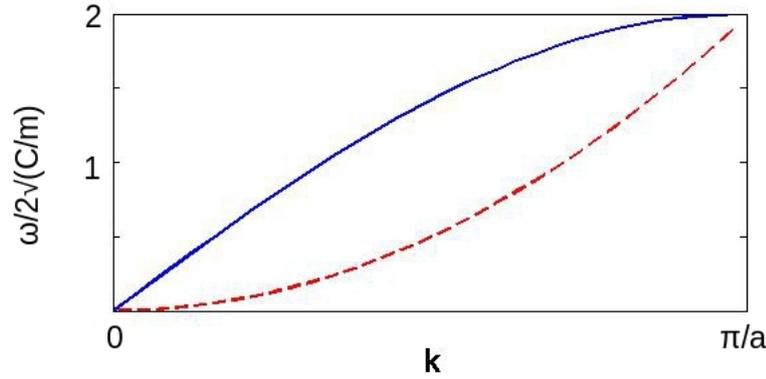
Figure 3.2: The dispersion relation derived from the spring model (solid blue line), and the dispersion relation for the flexural vibration of a thin plate (dashed red line).

Figure 3.1. Considering the atom n at position u_n, we see that the force on this atom depends only on the distance to the neighbouring atoms, giving the equation of motion

$$m\ddot{u}_n = C(u_{n+1} - 2u_n + u_{n-1}). \qquad (3.1)$$

We are looking for solutions in the form of travelling waves, so we make the assumption $u \propto e^{ikn-i\omega t}$, where k is a wavenumber and ω a frequency, and obtain

$$-m\omega^2 = 2C[\cos(k) - 1], \qquad (3.2)$$

which gives the dispersion relation

$$\omega = 2\sqrt{\frac{C}{m}}|\sin(k/2)|. \qquad (3.3)$$

This dispersion relation is plotted in Figure 3.2 (blue solid line), where it can be seen that it is nearly linear for small wavenumbers.

In the three-dimensional case, the scalar spring constant is replaced with a 3×3 matrix, known as the dynamical matrix, where each element is given by the second derivative of the total energy with respect to the positions of the interacting atoms.
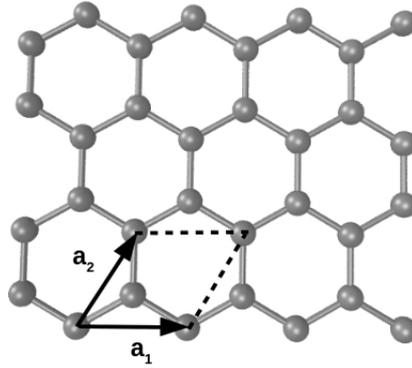
Figure 3.3: Lattice structure of graphene, with the lattice vectors $\mathbf{a}_1$ and $\mathbf{a}_2$ indicated by arrows.

In this case, the equations of motion have three sets of solutions on the form $\mathbf{u}_n \propto \vec{\varepsilon} e^{i\mathbf{k}\cdot\mathbf{R} - i\omega t}$, where $\vec{\varepsilon}$ is the polarization vector. The three sets of solutions correspond to three vibrational modes. Two of the modes will be transverse, with polarization vectors perpendicular to the wavevector $\mathbf{k}$, while the third is a longitudinal mode where the polarization vector and wavevector are parallel. These three modes are often called normal modes [1].

If there are two atoms in the lattice unit cell instead, the number of normal modes will increase to six. Three of these modes will be acoustic modes where the atoms in the unit cell move in the same direction, and three will be optical modes where the atoms move in opposite directions.

Now, instead of the three-dimensional crystal lattice, picture a suspended graphene sheet. The unit cell in graphene contains two atoms, as can be seen in Figure 3.3, resulting in six normal modes. Two of these must be longitudinal modes, one acoustic and one optical, which are similar to the longitudinal modes in a three-dimensional crystal. There is also one acoustic and one optical transverse mode where the atoms still move in the graphene plane. However, there must also be a pair of transverse modes where the atoms are displaced in a direction normal to the graphene plane, as illustrated in Figure 3.4. These modes, which are called flexural modes, behave quite differently compared to the in-plane phonon modes.

One might think that we could use the simplified model with atoms connected by springs to understand the flexural mode as well, but in fact this model will fail, particularly for the interesting case of long wavelengths. The reason is that the spring model only depicts stretching motions which alter the bond lengths of the material. In flexural motion, however, the main distortion of the material is bending rather than stretching. The bending is also associated with an increase in energy and thus with a force on the atoms directed towards the equilibrium position. However, as this bending energy is related to the changes in bond angles between atoms rather than to changes in the bond lengths, a model depicting this motion would have to include more long-ranged interactions, at least with second nearest neighbours. It

Figure 3.4: Graphene with atoms displaced in the out-of-plane direction, as in flexural vibrations.

is therefore more difficult to construct a simple atomistic model that describes the origin of this energy.

Instead of an atomistic model, we turn to continuum mechanics to understand the flexural acoustic mode. We regard the graphene sheet as a thin plate. For a thin plate, the bending energy E_b is proportional to the square of the curvature of the material [62], so that

$$E_b = \frac{\kappa}{2}|\nabla^2 w|^2, \tag{3.4}$$

where w is the out-of-plane displacement and κ is the bending rigidity of the material. This leads to an equation of motion of the form

$$\rho\ddot{w} + \kappa\Delta^2 w = 0, \tag{3.5}$$

where ρ is the two-dimensional density of the plate. Assuming a propagating wave solution, we set $w \propto e^{i\mathbf{k}\cdot\mathbf{R}-i\omega t}$ and obtain the dispersion relation

$$\omega = |\mathbf{k}|^2\sqrt{\frac{\kappa}{\rho}}. \tag{3.6}$$

The out-of-plane or flexural mode thus has a quadratic dispersion relation, rather than the linear dispersion relation displayed by the in-plane modes in graphene and by phonons in three-dimensional materials. A plot of this dispersion relation against the wavevector magnitude $k = |\mathbf{k}|$ can be seen in Figure 3.2. Since the group velocity is given by $\partial\omega/\partial k$, it is clear that the flexural phonons will have a lower group velocity than the in-plane phonons at long wavelengths. The group velocity for the flexural phonons will also change considerably with k even at long wavelengths, while that of the in-plane phonons is almost constant.

Although the bending energy in graphene is mainly related to changes in bond angles, out-of-plane distortions are in general also accompanied by stretching of the interatomic bonds. This means that an out-of-plane distortion changes the strain in the material. If we again regard the graphene sheet as a thin plate, it can be shown that the stretching couples the flexural vibrations to the in-plane modes and introduces nonlinear terms in the equations of motion for the flexural displacement [62]. This geometric nonlinearity is responsible for some of the special properties of graphene, for example the negative thermal expansion coefficient that will be discussed in the next section.
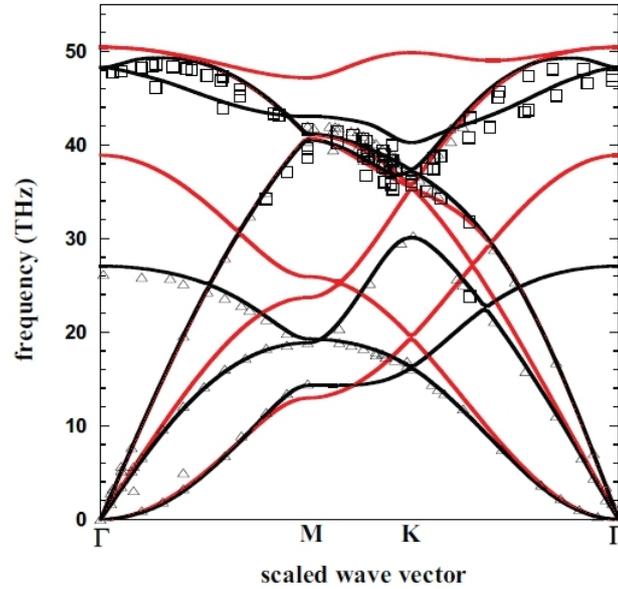
Figure 3.5: Phonon dispersion of graphene as calculated using density functional pertuba-tion theory (black lines) and the bond-order potential used in Papers IV and V (red lines). The symbols represent experimental results. Reprinted with permission from Ref. [63]. Copyright 2014 by the American Physical Society.

At this point, one might ask how well the two simple models we have used to derive phonon dispersion relations reproduce the phonon dispersion in graphene. The phonon dispersion of graphene as obtained from experiments and from atomistic simulations can be seen in Figure 3.5. At small wavenumbers, *i.e.* close to the Γ point in the figure, we see that three of the phonon modes have frequencies approaching zero. These are the acoustic modes. Two of these, the longitudinal and transverse modes, clearly have an approximately linear dispersion close to the Γ point, as in the simplified model. The third is the flexural acoustic mode, which can be seen to have an approximately quadratic dispersion. Our simple models thus give us a good general idea of the behaviour of the acoustic phonon modes. The dispersion relations of the optical modes are also included and we can see that these modes have considerably higher frequencies than the acoustic modes at the Γ point.

Apart from determining the group velocity, the dispersion relation also affects the number of phonons in the vibrational mode. To see how, we must recall that while the classical description of lattice vibrations given above works well for most cases, phonons follow the rules of quantum mechanics. As phonons are bosons, the probability that a phonon state is occupied is given by the Bose-Einstein distribution

$$n_{\mathrm{BE}}(\varepsilon) = \frac{1}{e^{(\varepsilon-\mu)/k_{\mathrm{B}}T} - 1},$$ (3.7)

where $\varepsilon = \hbar\omega$ is the phonon energy, μ is the chemical potential, which is always zero

for phonons, T is the temperature and k_B is Boltzmann's constant. As an example we will consider the limit $\omega \to 0$, in which case the exponential term can be expanded and we obtain

$$n_{BE} \approx \frac{k_B T}{\hbar \omega} \tag{3.8}$$

The number of phonons at a given frequency is given by multiplying the distribution function with the density of states $D(\omega)$, which for a two-dimensional system depends on the wavenumber and dispersion relation according to

$$D(k) = \frac{k}{2\pi} \frac{1}{\partial \omega / \partial k}. \tag{3.9}$$

For the flexural acoustic mode, it is clear from Equation 3.6 that this leads to

$$D(\omega) = \frac{1}{4\pi \sqrt{\kappa/\rho}}. \tag{3.10}$$

The in-plane acoustic modes have dispersion relations similar to those of phonons in three-dimensional materials. As we see in Figures 3.2 and 3.5, this means that they have nearly linear dispersion at low frequencies, and we therefore make the approximation $\omega(k) \approx v_g k$. The constant v_g is the group velocity. This leads to the density of states

$$D(\omega) = \frac{\omega}{2\pi v_g^2}. \tag{3.11}$$

Multiplying the density of states for acoustic in-plane and flexural phonons with the distribution function, we see that the number of phonons in the flexural modes becomes proportional to ω^{-1} as $\omega \to 0$, while the number of phonons in the in-plane modes approach a constant value. This means that there will be more flexural than in-plane acoustic phonons at low frequencies. In fact, using values of κ, ρ and v_g appropriate for graphene it has been calculated that the flexural acoustic phonons should be more abundant than in-plane acoustic phonons over a large frequency range [64].

3.1.2 Anharmonicity and thermal properties

The harmonic approximation for the interaction between atoms can provide a general description of phonon behaviour, but some important material properties are connected to the deviations from a harmonic potential. For most materials, thermal expansion and phonon thermal conductivity are determined by the anarmonicity of the interatomic interactions. In graphene, this is true for the in-plane phonon modes, while the flexural mode is also affected by the geometric nonlinearity discussed in the previous section. The thermal properties of graphene are mainly determined by the acoustic phonon modes, and this section will therefore focus on acoustic phonons.

The degree of anharmonicity of a phonon mode can be quantified in terms of the Grüneisen parameter $\gamma(\mathbf{k})$, which measures how the phonon frequencies change

if the volume of the unit cell changes. The Grüneisen parameter for each phonon mode can be calculated as

$$\gamma(\mathbf{k}) = -\frac{V}{\omega(\mathbf{k})}\frac{\partial\omega(\mathbf{k})}{\partial V} \tag{3.12}$$

where V is the volume of the unit cell. For a two-dimensional material like graphene, the volume is replaced by an area. It is important to note that the Grüneisen parameter captures not only the anharmonicity of the interatomic interactions but also the geometric nonlinearity of the flexural mode. The total Grüneisen parameter of a material can be calculated as an average of the Grüneisen parameters of the individual vibrational modes, and is directly related to the thermal expansion coefficient [1].

In graphene, the flexural acoustic mode has been found to have a large and negative Grüneisen parameter. This is due to the geometric nonlinearity, which causes the frequency of the flexural mode to increase as the unit cell is expanded in much the same way as stretching a piano string causes the tone it emits to change. As the frequency increases with increasing unit cell area, the sign of the derivative in Equation 3.12 is positive and the constant itself becomes negative. In a theoretical study by Mounet and Marzari [65] the Grüneisen parameter of the flexural acoustic mode was found to reach -80 at low frequencies, where the other modes display more modest values between 0 and 2. The flexural acoustic mode thus dominates the average Grüneisen parameter of the material at low temperatures, and the negative sign results in a negative thermal expansion coefficient for graphene at low and moderate temperatures [65,66]. The negative thermal expansion coefficient has also been confirmed experimentally, see *e.g.* Ref. [67].

Thermal conductivity

Both the anharmonicity of the interatomic interactions and the geometric nonlinearity also impede the phonon transport by causing phonon-phonon scattering to occur, which affects the phonon thermal conductivity. In fact, the type of phonon transport in a sample depends on the relation between the sample size and the mean free path of the phonons between scattering events. If the sample size is similar to or smaller than the mean free path, the thermal conductivity will mainly be limited by phonons scattering against the edges of the material. This is termed ballistic thermal transport. For sample sizes much larger than the mean free path, on the other hand, phonon-phonon scattering becomes more important and the length of the mean free path determines the intrinsic phonon thermal conductivity. This is known as diffusive transport. The total thermal conductivity is also influenced by extrinsic factors, such as phonon scattering against defects.

For a three-dimensional material in the diffusive limit, phonon-phonon scattering processes affect the phonon thermal conductivity in such a way that it becomes independent of the sample size, even if there are no defects or edges. Theoretical studies suggest that this is not the case in materials of a lower dimensionality. For one-dimensional materials the thermal conductivity seems to have a power-law dependence on the sample size, and for two-dimensional crystals it has been claimed

that the thermal conductivity increases as $\ln N$, where N is the number of atoms (see [68] and references therein). The models for two-dimensional lattice conductivity emphasize the importance of long-wavelength acoustic phonons, which are weakly scattered in two-dimensional lattices.

In graphene, acoustic phonons are the main heat carriers [69, 70]. Experimental studies of the thermal conductivity of suspended graphene have found it to be high, between 2000 and 5000 W/mK [68, 69, 71]. In line with the theoretical results for general two-dimensional lattices, this high thermal conductivity has been attributed to long-wavelength in-plane acoustic modes, which are weakly scattered and hence have long mean free paths. Theoretical calculations of the thermal conductivity have also been successful in reproducing the experimental thermal conductivity values when assuming that the in-plane acoustic phonons are the main heat carriers [68, 72, 73]. In these studies, flexural acoustic phonons have been considered to contribute very little to the thermal conductivity due to their small group velocity and large Grüneisen parameter, which indicates strong scattering.

However, some of the approximations made in these theoretical studies have been questioned [74]. In particular, it has been pointed out that due to the symmetry of graphene there exists a selection rule preventing any scattering process involving an uneven number of flexural phonons [63, 64, 75]. This means that although the large Grüneisen parameter of the flexural mode indicates strong scattering, many of the scattering processes are in fact forbidden and the lifetimes and mean free paths of the flexural phonons are therefore quite large. Theoretical studies that take these scattering rules into account find that flexural acoustic phonons dominate the thermal conductivity of graphene [63, 64]. Experimental results also appear to support this conclusion [76, 77].

Interestingly, the logarithmic dependence of the thermal conductivity of a two-dimensional crystal on sample size has gained support from experimental measurements on graphene, where the thermal conductivity was seen to increase for sample sizes up to 9 μm [78]. However, there are also theoretical studies that suggest that the observed length dependence is a consequence of the long phonon mean free paths in graphene. These studies indicate that the transport is still partly ballistic in the micrometre-sized samples and that the thermal conductivity does in fact converge for even larger samples where purely diffusive transport can be observed [79, 80].

Finally, the thermal conductivity of graphene is also strongly affected by defects, edges and substrates. The thermal conductivity of graphene on a substrate has been observed to be 600 to 1000 W/mK, which is substantially lower than for suspended graphene but still higher than that of *e.g.* silicon [68]. Substrates, as well as edges, point defects and grain boundaries, may make it possible to tune the thermal conductivity of graphene. This may be useful in applications such as thermoelectrics where a lower thermal conductivity is advantageous [68].
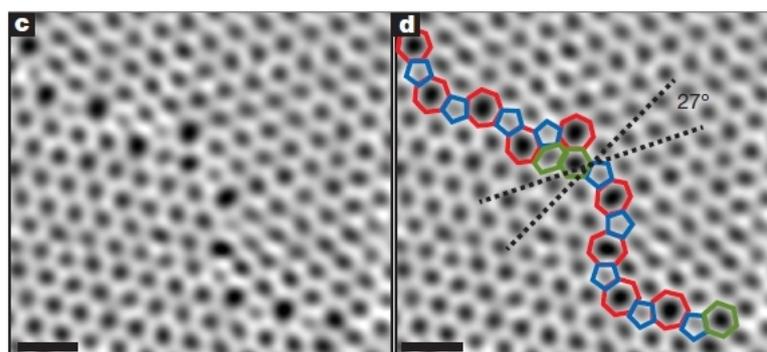
Figure 3.6: TEM image of a graphene grain boundary with $27°$ misorientation angle. In the right-hand image the defect structure of the grain boundary is indicated. Figure reprinted by permission from Macmillan Publishers Ltd: Nature, Ref. [81], copyright 2011.

3.2   Grain boundaries in graphene

As mentioned in the previous section, the two-dimensional nature of graphene means that the atoms can be displaced in the direction perpendicular to the graphene sheet, and these displacements are accompanied by a different energy cost compared to in-plane displacements. This fact is significant also with regard to grain boundaries.

The most obvious difference between a grain boundary in graphene and a grain boundary in an ordinary three-dimensional material is the dimensionality. In a three-dimensional crystal, the grain boundaries are two-dimensional defects, but in graphene the grain boundaries are by necessity one-dimensional. A consequence of this is that there are no twist grain boundaries in graphene, as all rotations of the grains must be around an axis perpendicular to the graphene sheet.

3.2.1   Grain boundary structure

Graphene grain boundaries are found in graphene grown by chemical vapour deposition, where they occur as a result of the single-crystal grains growing from different nucleation centers having different orientations [82]. Where the grains meet, grain boundaries are formed. TEM studies of graphene grain boundaries reveal that they consist of non-hexagonal carbon rings, mainly alternating pentagon and heptagon defects [81, 83], as can be seen in Figure 3.6. This is also observed in several theoretical investigations of grain boundary structure [84–86].

In graphene, a heptagon and a pentagon situated close together in the lattice form an edge dislocation. Edge dislocations are equivalent to adding a semi-infinite strip of atoms to the material, with the actual dislocation core forming at the end of the strip (see Figure 3.7). The presence of the dislocation distorts the graphene lattice, introducing a strain into the material. However, the energy cost of in-plane stretching or compression of graphene is quite high, as evidenced by the two-dimensional elastic stiffness being about 340 N/m, corresponding to a Young's modulus of 1
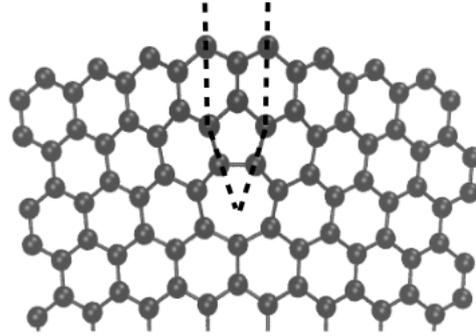
Figure 3.7: A dislocation in a graphene sheet. Dashed lines indicate the "added" strip of carbon atoms.

TPa [87]. In contrast, the bending rigidity κ is only about 2×10^{-19} J. The strain introduced by the dislocation will therefore cause the graphene sheet to bend, and dislocations in graphene are thus accompanied by out-of-plane distortions, or buckling, of the graphene sheet. This has also been observed experimentally [88–90].

Since grain boundaries consist of alternating pentagon and heptagon defects, they can be viewed as an array of dislocations. Computational studies of graphene grain boundaries have revealed that they do indeed cause out-of-plane buckling, as illustrated in 3.8(a), and that this can reduce the formation energy of the grain boundary considerably [84–86]. Furthermore, the degree of buckling has been found to depend on the misorientation angle. Grain boundaries with misorientation angles between $20°$ and $40°$ in particular have been found to cause smaller buckling. An example of this is the grain boundary with misorentation angle $32.2°$, which displays the highest possible defect density but no buckling (Figure 3.8(b)).

In addition to ordinary tilt grain boundaries, grain boundaries with zero tilt angle have also been observed. These zero-angle grain boundaries occur at the border between two regions that have the same orientation but a translational mismatch. They typically consist of pentagon and octagon defects [82].

3.2.2   Grain boundaries and material properties

By breaking the lattice symmetry and inducing out-of-plane deformations, grain boundaries can be expected to change the properties of graphene. The effect of grain boundaries on the mechanical and electronic properties of graphene have been a subject of intense study, and copious amounts of information exist on these topics. Here, we will only touch upon the main points.

The mechanical properties of polycrystalline graphene have been studied both theoretically and in nanoindentation experiments, where the elastic modulus and fracture load can be determined [82]. Early experimental studies found a significant reduction in strength of polycrystalline graphene compared to single-crystal films.

(a)

(b)
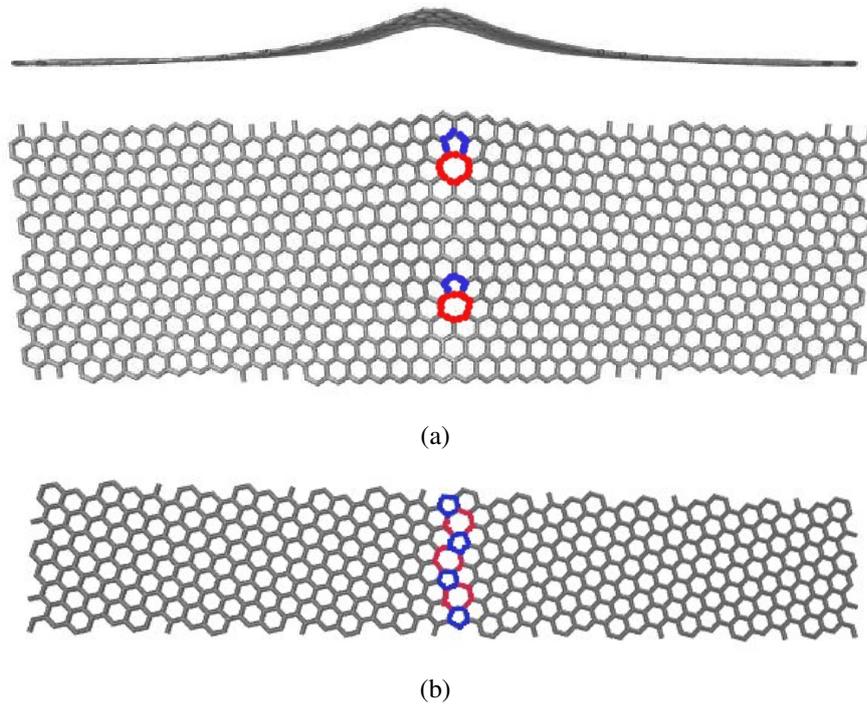
Figure 3.8: (a):A grain boundary with misorientation angle 9.4°, viewed from an in-plane direction (upper image) and from the direction perpendicular to the graphene sheet (lower image). This grain boundary clearly displays out-of-plane buckling. The dislocations are indicated in red (heptagon) and blue (pentagons). (b): A grain boundary with misorientation angle 32.2°.

However, Lee et al. [91] observed that the measured strength was influencend by the technique used to fabricate the samples and that polycrystalline graphene could be almost as strong as single crystals, especially in samples with large grains. However, indentation tests on grain boundaries yielded fracture loads 20 to 40 % lower than the fracture load in the middle of a grain [91].

In theoretical studies, it has been found that the strength of a grain boundary depends on the misorientation angle. Grain boundaries with large misorientation angles appear to be stronger than grain boundaries with smaller misorientation angles, something that has also been seen in some experimental studies (see [82] and references therein). Meanwhile, theoretical studies of realistic grain boundary networks have indicated that the fracture load decreases and the Young's modulus increases with increasing grain size, and also that points where two grain boundaries meet serve as starting points for crack formation [92].

The electron transport in polycrystalline graphene has been investigated experimentally. It was found that the electron mobility and conductivity was lower in the polycrystalline samples than in pristine graphene. Scanning probe measurements at individual grain boundaries also find lowered conductivity [82]. In theoretical studies, it has been found that the defect structure at the grain boundary influences the electron transmission, with complete reflection occuring for some grain boundaries and electron energies. An increase in conductivity with increasing grain size has also been predicted [82].

In addition to electronic and mechanical properties different from those of perfect graphene, grain boundaries also display an increased reactivity. It has been seen that both oxygen and hydrogen adsorb preferentially to grain boundaries, something that may for instance alter the electron transport properties of the boundary and could be important in chemical sensing applications [92]. Also, theoretical investigations have predicted that several metals adsorb more strongly to pentagon and heptagon defects, as well as to Stone-Wales defects, than to pristine graphene [93–97]. A Stone-Wales defect contains two pentagons and two heptagons, as can be seen in Figure 3.9, and arises due to rotation of a carbon-carbon bond. The preferential adsorption of metals to pentagon and heptagon defects imply that metals could also adsorb more strongly to grain boundaries than to pristine graphene. If this is the case, it may be important for example in the context of graphene being used as a support for nanoparticle catalysts. The possibility of studying metal adsorption on graphene grain boundaries using model potentials is further discussed in Chapter 6.

Grain boundaries in graphene also affect the thermal transport, something that is of particular interest here as it involves phonon scattering. Thermal transport across grain boundaries in graphene has mainly been investigated in theoretical and computational studies, often using non-equilibrium molecular dynamics or Green's function methods [98–101]. In these studies, grain boundaries in graphene are found to have a high thermal conductivity compared to grain boundaries in other materials. Some molecular dynamics studies also find that the thermal conductivity across the grain boundary decreases with increasing misorientation angle between the grains, probably due to an increase in defect density [98,99]. However, the Green's function
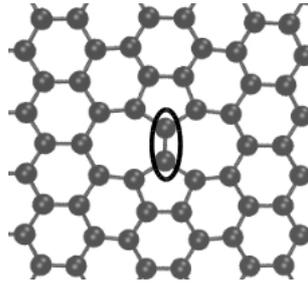
Figure 3.9: A Stone-Wales defect, with the rotated bond indicated by an ellipse.

study by Lu et al. [100] found no evidence for such a trend.

Interestingly, none of the theoretical studies of thermal conductivity across grain boundaries make any mention of out-of-plane buckling close to the boundary. The only study which does consider such effects is focused on thermal conductivity along the boundary [102]. It is possible that no grain boundary buckling was observed in some of these studies due to the way in which the grain boundaries were constructed. In all probability, the presence of out-of-plane buckling influences the thermal conductivity, as out-of-plane distortions due to compressive strain has been found to affect the thermal transport [103]. Also, the buckling can be shown to be the main cause of scattering of long-wavelength flexural phonons, as is further discussed in Chapter 6 and Papers IV and V.

Chapter 4

Computational Methods

The research presented in this thesis has been carried out using computational models of the studied materials. In this chapter, a brief introduction to the computational methods is given. Two of the methods treated here describe the atomic structure of the materials, while in the third the studied material is treated as a continuum.

When using the first two methods, the aim is to understand the overall properties of the material based on the interactions between the atoms it contains. To accomplish this it is necessary to model the interactions in a realistic manner. The first method described here is density functional theory, in which the interatomic interactions are determined from the electron density. This method gives a relatively accurate description of material properties, but is quite computationally demanding. In the second method, the interatomic interactions are described by a potential that is parametrized by fitting to either experimental or first-principles results. This is less computationally demanding than the density functional approach but also gives a less accurate description of the interatomic interactions.

In this thesis, density functional theory has been used in the investigation of defect segregation to grain boundaries of barium zirconate. Interatomic model potentials have been used both when studying barium zirconate and in the modelling of graphene, while the continuum mechanical modelling is applied only to graphene.

4.1 Density functional theory

Density functional theory was developed as a way to solve the Shrödinger equation,

$$H\Psi(\mathbf{r}_1, \mathbf{r}_2...; \mathbf{R}_1, \mathbf{R}_2...; t) = E\Psi(\mathbf{r}_1, \mathbf{r}_2...; \mathbf{R}_1, \mathbf{R}_2...; t), \qquad (4.1)$$

for a large number of atoms. Here, $\Psi(\mathbf{r}_1, \mathbf{r}_2; ..., \mathbf{R}_1, \mathbf{R}_2...; t)$ is the quantum mechanical wavefunction describing the system, $\mathbf{r}_i$ is the position of electron i and $\mathbf{R}_I$ is the position of nucleus I. E is the total energy corresponding to the wavefunction Ψ and

H is the system Hamiltonian

$$H = -\frac{1}{2}\sum_i \nabla_i^2 + \frac{1}{2}\sum_{i\neq j}\frac{1}{|\mathbf{r}_i - \mathbf{r}_j|} - \sum_{i,I}\frac{Z_I}{|\mathbf{r}_i - \mathbf{R}_I|} \tag{4.2}$$
$$-\frac{1}{2}\sum_I \frac{\nabla_I^2}{M_I} + \frac{1}{2}\sum_{I\neq J}\frac{Z_I Z_J}{|\mathbf{R}_I - \mathbf{R}_J|},$$

where Z_I and M_I are the charge and mass of nucleus I. The electron mass does not appear as the Hamiltonian is expressed in Hartree atomic units, where both the electron mass and the elementary charge are unity by definition. The number of terms in this Hamiltonian, and the complexity of the problem, increases quickly with the number of particles in the system. For a small system such as a hydrogen atom it can be solved. However, just a single unit cell of barium zirconate brings five nuclei and 120 electrons, increasing the complexity significantly, and for larger systems the problem is in general intractable.

The first step to reducing the complexity of this problem is to take advantage of the fact that the nuclei are much more massive than the electrons. Even the hydrogen nucleus, which consists of a single proton, is about 1800 times heavier than an electron. Since the forces affecting electrons and nuclei are approximately of the same strength, this implies that the nuclei will move much more slowly than the electrons. The electrons can thus be assumed to follow the nuclear motion adiabatically, that is to remain in the ground state as the positions of the nuclei change [104]. It is therefore possible to separate the electronic and nuclear parts of the problem, and to solve the electronic problem for specific configurations of immobile nuclei. This is known as the Born-Oppenheimer approximation [105].

When applying the Born-Oppenheimer approximation, the effect of the nuclei on the electrons can be expressed as an external potential V_{ext}. The Hamiltonian is then reduced to

$$H = -\frac{1}{2}\sum_i \nabla_i^2 + \sum_{i\neq j}\frac{1}{|\mathbf{r}_i - \mathbf{r}_j|} + V_{\text{ext}}. \tag{4.3}$$

However, even with this simpler Hamiltonian a substantial complexity remains. In particular, the electron-electron interactions described by the second term require all electrons in the system to be treated simultaneously. It is possible to obtain an exact solution to the Schrödinger equation with this Hamiltonian for the hydrogen atom, and for small molecules an exact numerical solution may be found [104], but for other systems a different approach is needed.

4.1.1 Hohenberg-Kohn theorems

The quantum mechanical wavefunction for a system of interacting electrons is a function of the positions of all electrons in the system. In density functional theory, the problem of determining this wavefunction is replaced by the problem of finding the electron density of the ground state, which simplifies the problem considerably

as the electron density is only a function of the three spatial coordinates. The motivation for this replacement is found in two theorems that were proven by Hohenberg and Kohn in 1964 [106, 107]. The first theorem states that a given ground state electron density $n_0(\mathbf{r})$ can only result from one specific external potential V_{ext}. If the ground state density is known, the potential is therefore determined up to an additive constant. This in turn means that all properties of the system are determined implicitly by the electron density.

The second theorem concerns the relation between the energy and the ground state electron density. For a system with electron density $n(\mathbf{r})$, the energy can be expressed as a functional of the density according to

$$E[n(\mathbf{r})] = F[n(\mathbf{r})] + \int n(\mathbf{r}) V_{\text{ext}}[n(\mathbf{r})] d\mathbf{r}, \tag{4.4}$$

where $F[n(\mathbf{r})]$ contains the kinetic energy and contributions from electron-electron interactions. The second Hohenberg-Kohn theorem states that the ground state electron density $n_0(\mathbf{r})$ is the electron density that minimizes the energy functional, so that

$$E_0 = E[n_0(\mathbf{r})] = \min_{n(\mathbf{r})} E[n(\mathbf{r})], \tag{4.5}$$

where E_0 is the ground state energy. The task of finding the ground state electron density is thus equivalent to minimizing the energy functional. However, this is still a challenge as the functional is not known, chiefly because of the contribution from electron-electron interactions.

4.1.2 The Kohn-Sham equations

In order to bring the problem closer to a solution, the unknown functional $F[n(\mathbf{r})]$ can be divided into three terms,

$$F[n(\mathbf{r})] = T_{\text{s}}[n(\mathbf{r})] + E_{\text{H}}[n(\mathbf{r})] + E_{\text{xc}}[n(\mathbf{r})], \tag{4.6}$$

as suggested by Kohn and Sham in 1965 [107, 108]. Here, $T_{\text{s}}[n(\mathbf{r})]$ is the kinetic energy of a system of noninteracting electrons and the Hartree energy

$$E_{\text{H}}[n(\mathbf{r})] = \frac{1}{2} \int \frac{n(\mathbf{r})n(\mathbf{r}')}{|\mathbf{r} - \mathbf{r}'|} d\mathbf{r} d\mathbf{r}' \tag{4.7}$$

is a mean-field approximation of the electrostatic interaction between electrons. Both these terms are known exactly. The third term is the exchange-correlation functional, which contains the many-body contributions to the kinetic energy, exchange effects related to the Pauli principle and correlation effects due to the electrostatic repulsion.

As the term representing the kinetic energy of a system of noninteraction electrons can now be separated from the rest of the functional, it is possible to replace

the original system with an equivalent system of noninteracting electrons moving in an effective potential given by

$$V_{\text{eff}}(\mathbf{r}) = V_{\text{H}}(\mathbf{r}) + V_{\text{xc}}(\mathbf{r}) + V_{\text{ext}}(\mathbf{r}), \tag{4.8}$$

where $V_{\text{H}} = \int (n(\mathbf{r}')/|\mathbf{r}-\mathbf{r}'|)d\mathbf{r}'$ is the Hartree contribution and $V_{\text{xc}} = \delta E_{\text{xc}}[n(\mathbf{r})]/\delta n(\mathbf{r})$. The system of independent electrons is then described by the Kohn-Sham equations,

$$\left[-\frac{1}{2}\nabla^2 + V_{\text{eff}} \right] \phi_i(\mathbf{r}) = E_i\phi_i(\mathbf{r}), \tag{4.9}$$

where $\phi_i(\mathbf{r})$ and E_i are the wavefunction and energy eigenvalue of the one-electron state i. The wavefunctions ϕ_i are also known as Kohn-Sham orbitals. The total electron density is obtained as $n(\mathbf{r}) = \sum_i f_i|\phi_i|^2$, where f_i is the occupation number of the one-electron state, and the energy corresponding to this electron density is given by

$$E = \sum_i f_iE_i - E_{\text{H}}[n(\mathbf{r})] + E_{\text{xc}}[n(\mathbf{r})] - \int n(\mathbf{r})V_{\text{xc}}(\mathbf{r})d\mathbf{r}. \tag{4.10}$$

Since $V_{\text{H}}(\mathbf{r})$ depends on the electron density, the Kohn-Sham equations have to be solved iteratively. An initial guess will be used as a starting point for the density. The equations will then be solved to obtain a new density, which is used in the next iteration. This process has to be repeated until the solution is self-consistent, *i.e.* the calculation results in the same electron density that was used as input.

So far no approximations have been made, and with the exact exchange-correlation functional the problem could be solved exactly. However, the exchange-correlation functional is not known. Instead, density functional theory calculations rely on approximations. Common approximations to the exchange-correlation functional, as well as some other topics in the practical implementation of density-functional calculations, are discussed in the next section.

4.1.3 Practical implementation

Exchange-correlation functionals

The first approximate exchange-correlation functional was suggested by Kohn and Sham in their original paper on density functional theory [108]. It is called the local density approximation, or LDA, and uses the exchange and correlation functionals of a homogeneous electron gas. For the homogeneous electron gas, the energy density ε_{x} resulting from exchange is known exactly and the energy density ε_{c} resulting from correlations can be obtained from Monte Carlo simulations [109]. The combined exchange and correlation energy density can be taken to be $\varepsilon_{\text{xc}} = \varepsilon_{\text{x}} + \varepsilon_{\text{c}}$. Under the LDA approximation, the exchange and correlation energy density of the studied system at a point $\mathbf{r}$ is approximated by that of a homogeneous electron gas with the same electron density as the density at point $\mathbf{r}$. The functional can then be obtained from

$$E_{\text{xc}}[n(\mathbf{r})] = \int n(\mathbf{r})\varepsilon_{\text{xc}}[n(\mathbf{r})]d\mathbf{r}. \tag{4.11}$$

The LDA has been quite successful at reproducing *e.g.* bond lengths and vibrational frequencies, especially for systems with slowly varying electron densities [104]. It also has the advantage of being fairly uncomplicated. However, the binding energies between atoms are often overestimated by LDA [110] as it produces electron densities that are too homogeneous. Systems with strongly correlated electrons are also poorly reproduced [104].

Several attempts have been made to develop functionals that perform better than the LDA. Many of these attempts aim to take inhomogenieties in the electron density into account by making the exchange-correlation energy density a function of both the local electron density and the local gradient of the electron density. Such functionals are called generalized gradient approximations, or GGA, and they are broadly divided into two categories depending on if the functionals have been parametrized by fitting to experimental data, or by requring adherence to formal conditions such as sum rules or long-ranged decay [104]. The GGA functional used for most of the density functional calculations in this thesis is called the PBE (Perdew-Burke-Ernzerhof) and it belongs to the second category [111].

Although GGA is an improvement over LDA in some areas, there are problems that remain. One problem that is common to both LDA and GGA is that they underestimate the band gap in insulators and semiconductors quite substantially. The band gap calculated in density functonal theory has two contributions. The first contribution is simply the difference in energy between the lowest unoccupied Kohn-Sham orbital and the highest occupied Kohn-Sham orbital. The second contribution arises from a discontinuity in the exchange-correlation potential V_{xc}. Both GGA and LDA lack this discontinuity, erroneously setting the second contribution to the band gap to zero. This will affect the calculated formation energies of defects if the defect formation involves introducing an electron in a previously unoccupied state. Segregation energies are less affected as they are the difference between two formation energies, and most of the error will therefore cancel.

Basis sets

When solving the Kohn-Sham equations, it is necessary to construct a mathematical representation of the one-electron wavefunctions. Normally, this is done by expanding the wavefunctions using a basis set, thereby transforming the equation into a linear eigenvalue problem. The choice of basis set is usually made based on the system geometry and properties. For crystalline materials, which can be represented by a small repeating unit cell, it is natural to use plane waves as the basis set. According to Bloch's theorem [112], the one-electron wavefunction can then be expressed as

$$\phi_{n,\mathbf{k}}(\mathbf{r}) = u_{n,\mathbf{k}}(\mathbf{r})e^{i\mathbf{k}\cdot\mathbf{r}}, \tag{4.12}$$

where n is the index of the wavefunction, $\mathbf{k}$ is a wave vector in the first Brillouin zone of the unit cell and $u_{n,\mathbf{k}}(\mathbf{r})$ is a function with the same periodicity as the studied system. The periodic function can be expanded in a Fourier series using the

reciprocal lattice vectors $\mathbf{G}$:

$$u_{n,\mathbf{k}}(\mathbf{r}) = \sum_{\mathbf{G}} c_{n,\mathbf{k}+\mathbf{G}} e^{i\mathbf{G}\cdot\mathbf{r}}, \qquad (4.13)$$

where $c_{n,\mathbf{k}+\mathbf{G}}$ are expansion coefficients. The wavefunction can thus be expressed as a sum over all reciprocal lattice vectors, according to

$$\phi_{n,\mathbf{k}}(\mathbf{r}) = \sum_{\mathbf{G}} c_{n,\mathbf{k}+\mathbf{G}} e^{i(\mathbf{k}+\mathbf{G})\cdot\mathbf{r}}. \qquad (4.14)$$

Note that the inclusion of a Fourier series implies periodic boundary conditions. In principle, the sum includes an infinite number of reciprocal lattice vectors. In practice, it is customary to use a cutoff energy E_{cut}, so that for each wavevector $\mathbf{k}$ only reciprocal lattice vectors that fulfill the condition $\frac{1}{2}|\mathbf{k}+\mathbf{G}|^2 \leq E_{\mathrm{cut}}$ are included [104].

Studies of crystalline materials often involve systems where the crystalline translational symmetry is broken, such as systems with point defects or grain boundaries. In these cases, it is customary to construct a larger cell, termed a supercell, containing the defect. This approach makes it possible to model a defect in an extended material, but has some problems that will be discussed in Section 4.1.5.

Pseudopotentials

Using plane waves as a basis set for periodic systems has many advantages, but also a few disadvantages. A significant disadvantage is the slow convergence of the sum for rapidly varying wavefunctions. The electron wavefunctions tend to oscillate considerably close to the atomic nuclei, and describing these oscillations using a plane-wave basis set requires a high energy cutoff and is therefore computationally demanding.

The solution to this problem lies in that electrons that are likely to be found close to the atomic nucleus contribute little to the interatomic bonds, while the valence electrons that contribute strongly to the bonds are more likely to be found further from the nucleus. The valence and core electrons can thus be treated separately, in a way that lowers the required cutoff energy. A very common approach is to replace the potential caused by the nucleus and core electrons with a pseudopotential. At a distance from the atomic nucleus the pseudopotential generates wavefunctions that are the same as if all electrons were included in the calculation, while closer to the nucleus the wavefunctions are considerably smoother than in the all-electron case [113]. The smoother wavefunctions make it possible to use a lower cutoff energy, decreasing the computational cost.

4.1.4 Nuclear configuration

In the beginning of this brief overview of density functional theory, it was stated that the Born-Oppenheimer approximation can be applied to separate the motion

of electrons and nuclei, allowing us to focus solely on the system of electrons and include the nuclei in the form of an external potential. Having seen that the electronic problem may be solved, we now turn back to the issue of the nuclear configuration.

In density functional theory, the nuclei are usually treated classicaly. The justification for this is that the relatively large mass of the nuclei cause any quantum mechanical effects to be small. Since the total energy of the system of electrons and nuclei depends on the ionic positions, the force $\mathbf{F}_I$ on ion I can be found as the derivative of the total energy with respect to the position of the ion,

$$\mathbf{F}_I = -\frac{\partial E}{\partial \mathbf{R}_I}. \tag{4.15}$$

According to the Hellman-Feynman theorem, the derivative of the energy is equivalent to the expectation value of the corresponding gradient of the Hamiltonian, making it possible to obtain the force from the electron density [114]. The forces on the ions can be used to integrate the classical equations of motion and simulate the time evolution of the system, as is done in *ab initio* molecular dynamics. They can also be used with energy minimization algorithms to perform a geometry optimization of the system and find the ionic configuration corresponding to the lowest total energy [104].

4.1.5 Defects in periodic supercells

As seen in the discussion of basis sets, Section 4.1.3, the use of a plane-wave basis set imposes periodic boundary conditions on the system. As long as the translational symmetry of the material is perfect, this is unproblematic. However, if the symmetry is broken, for instance by the introduction of a defect, problems may arise. Applying periodic boundary conditions to a system with a defect can be thought of as modelling an infinite array of systems with identical defects. Unless the supercell is very large, the defect will interact with neighbouring defects in the array, that is, interact with itself through the periodic boundary conditions. This introduces errors into the calculation.

The easiest method of solution for this problem is to increase the size of the supercell until the defect energy no longer changes with supercell size, or if this is not possible, to calculate the defect energy for different supercell sizes and extrapolate to larger systems. However, for point defects attempts have also been made to find a general expression for the error introduced by defect self-interaction. In these attempts, the error is separated into a part arising from elastic interactions, *i.e.* the lattice distortion caused by the presence of the defect, and electrostatic interactions that occur if the defect is charged. For a cubic supercell with the side L, the elastic interaction has been found to be proportional to L^{-3} [115].

The electrostatic interaction requires a bit more consideration. Firstly, if the system contains a charged defect the supercell itself aquires a net charge, and in this case the periodic boundary conditions will lead to an infinite electrostatic energy. In calculations involving charged defects a uniform background charge of the same

magnitude as the defect charge but of opposite sign is therefore introduced into the supercell, keeping it charge neutral. Under these conditions, the error caused by the electrostatic interactions has been found to be proportional to L^{-1} [116, 117].

Several formulas for correcting the error introduced by the electrostatic interaction have been proposed (see *e.g.* [116–125]), although it has also been suggested that performing calculations for several different supercell sizes and extrapolating to the value for an infinite cell is a more reliable method [126]. A review of some of these correction schemes can be found in Ref. [127]. No correction schemes have been used in the present study. Although the calculations performed in Papers I to III do involve the energies of charged point defects, it is the segregation energy and not the formation energy that is calculated. As the segregation energy is the difference between two formation energies, most of the errors due to the periodic boundary conditions are expected to cancel. For higher-dimensional defects such as grain boundaries no correction schemes exist, and using supercells of different sizes is thus the only way to estimate the error.

Defect self-interaction can also occur in simulations carried out using interatomic model potentials, as periodic boundary conditions are often applied in these simulations in order to avoid introducing surfaces into the system. Since interatomic model potential simulations frequently use larger supercells than density functional theory calculations, the errors introduced by defect self-interaction tend to be less significant.

4.2 Interatomic model potentials

While density functional theory has many advantages, it also has the disadvantage of being computationally expensive. At present, systems containing up to 1000 atoms can be described with density functional theory, but for larger systems it is necessary to use less exact descriptions. Such descriptions are for example provided by interatomic model potentials, which are fitted to results from first-principles calculations or experiments. This is considerably less computationally expensive than density functional theory, but also less accurate.

As different types of interatomic interactions require different model potentials, there are many model potential types. The simplest are pair potentials, where the interaction between two atoms depends only on the distance between them. Such potentials are used to describe *e.g.* van der Waals or ionic interactions. Other potential types may include terms that depend on the relative positions of three to four atoms, or bond-order terms that describe covalent bonds.

In general, a single model potential cannot be assumed to give an adequate description of all interactions involving one chemical element in different surroundings. As an example, it is not possible to use the same potential to describe the oxygen atoms or ions in an oxide as to describe an oxygen molecule. This lack of transferability can cause problems, for example when attempting to calculate the formation energy of a material.

4.2.1 The Buckingham potential

To model barium zirconate the Buckingham potential has been used. The interatomic interactions in barium zirconate are mostly electrostatic, with contributions from van der Waals forces at small distances. This is reflected by the Buckingham potential, which has the form [128]

$$U_{ij}(r_{ij}) = Ae^{-r_{ij}/\rho} - \frac{C}{r_{ij}^6} + \frac{q_i q_j}{r_{ij}} \tag{4.16}$$

where q_i is the charge of ion i and A, ρ and C are constants. The exponential term represents Pauli repulsion, the second term describes van der Waals attraction and the third term is the long-ranged electrostatic interaction.

In some ionic materials, the polarizability of the ions is also significant for the interatomic interactions. When using model potentials, ionic polarizability can be incorporated through a shell model, as is done in Paper II. This means that the ion is treated as consisting of two parts, a massive core and a massless shell. The two parts are connected by a spring, allowing them to be displaced with respect to each other to a certain degree, and the charge of the ion is distributed over the two parts [129]. If the shell and core move in relation to each other this can displace the charge of the ion with respect to the mass, or even create a slight dipole moment, thus mimicking polarizability.

4.2.2 Bond-order potentials

For studying graphene, a bond order potential was used. Bond-order potentials were developed to describe semiconductors and other covalently bonded materials, and especially to reproduce different stacking sequences and crystal structures of the same material correctly with one single potential [130]. This is hard to achieve with ordinary pair potentials, which tend to predict the structure where the atoms have the highest coordination number (*i.e.* highest number of nearest neighbours) to be the most stable state. This is rarely correct for covalently bonded crystals. With the bond-order potential, the strength of the bonds to neighbouring atoms decreases as the coordination number increases, thus enabling the potential to reproduce more open structures.

The bond-order potential used here was originally developed by Tersoff [130]. In this potential, each bond between a pair of atoms i and j contributes to the total energy according to the potential

$$U_{ij} = f_C(r_{ij})[a_{ij}f_R(r_{ij}) + b_{ij}f_A(r_{ij})], \tag{4.17}$$

where f_R is a repulsive pair potential, a_{ij} is factor that limits the range of the repulsive potential, f_A is an attractive pair potential and f_C is a cutoff function that limits

interactions to the nearest neighbours. The pair potentials have the form

$$f_R(r) = Ae^{-\lambda_1 r}$$

$$f_A(r) = -Be^{-\lambda_2 r}$$

(4.18)

where A, B, λ_1 and λ_2 are constants. The remaining term in Equation 4.17, b_{ij}, is known as the bond-order term. It is given by

$$b_{ij} = (1 + \beta^n \xi_{ij}^n)^{-1/2n},$$

$$\xi_{ij} = \sum_{k \neq i,j} f_C(r_{ik}) g(\theta_{ijk}) e^{\lambda_3^3 (r_{ij} - r_{ik})^3},$$

$$g(\theta) = 1 + \frac{c^2}{d^2} - \frac{c^2}{[d^2 + (h - \cos\theta)^2]}.$$

(4.19)

Here, θ_{ijk} is the angle between the bonds $i - j$ and $i - k$. Although the first parametrization of the potential was done for silicon, a parameter set for carbon was later developed [131]. The potential was shown to reproduce the structures and cohesive energies of several carbon allotropes with reasonable accuracy. Recently, Lindsay and Broido have developed a new parameter set for carbon, aimed at giving a better description of the phonon dispersion [132]. This is the parameter set used in Papers IV and V.

Since the development of the Tersoff potential, efforts have been made to improve its performance further. Most well-known is perhaps the work of Brenner et al. [133, 134] and Stuart et al. [135], who aimed to improve the description of hydrocarbon molecules and intramolecular bonding. These attempts were quite successful and especially the Brenner potential is frequently chosen for modelling carbon structures.

Bond-order potentials of the Tersoff and Brenner types have also been used to describe the interactions between carbon and metals. It has been shown that if the angular dependence of the bond-order term is omitted, the functional form of the bond-order potentials is equivalent to that of the embedded atom model (EAM) potentials which are used to describe metals [136]. This potential form can thus be used to describe both carbon-carbon, metal-metal, and carbon-metal bonds. Such potentials describing the interactions of carbon with *e.g.* platinum, iron, cobalt, nickel and tungsten can be found in the literature [136–139].

4.2.3 Molecular dynamics simulations

With the total energy $E(\mathbf{R}_1, \mathbf{R}_2, ...)$ given by the interatomic potential as a function of the atom positions, the forces on the atoms can be obtained by differentiation according to

$$\mathbf{F}_i = -\frac{\partial E(\mathbf{R}_1, \mathbf{R}_2, ...)}{\partial \mathbf{R}_i}.$$

(4.20)

Knowledge of the forces may then be used to perform a classical molecular dynamics simulation, that is to investigate the time evolution of the system by integrating the equations of motion. Doing so produces a trajectory in phase space, and from this trajectory one can obtain information about the properties of the system. In general, molecular dynamics is used to model systems in equilibrium, and the studied quantitites are calculated as time averages over the phase space trajectory. To relate the obtained quantities to the macroscopic world, the time averages are assumed to be equivalent to the ensemble averages in statistical physics. Ensemble averages are by definition averages over several realizations of the same system, rather than over the time evolution of a single system. The assumption that a time average for one system is equivalent to an ensemble average is known as the ergodic hypothesis.

To perform molecular dynamics simulations in practice it is important to select an integration algorithm that is stable, conserves the total energy and is computationally inexpensive. The most common choice is the Verlet algorithm [140]. According to this algorithm, starting with particle i in position $\mathbf{R}_i(t)$ and with the velocity $\mathbf{v}_i(t)$, the position at the next timestep is

$$\mathbf{R}_i(t + \Delta t) = \mathbf{R}_i(t) + \mathbf{v}_i(t)\Delta t + \frac{1}{2}\mathbf{a}_i(t)\Delta t^2, \tag{4.21}$$

and the new velocity is calculated as

$$\mathbf{v}_i(t + \Delta t) = \mathbf{v}_i(t) + \frac{1}{2}[\mathbf{a}_i(t) + \mathbf{a}_i(t + \Delta t)]\Delta t, \tag{4.22}$$

where Δt is the timestep and $\mathbf{a}_i(t)$ is the acceleration. The acceleration is obtained from

$$\mathbf{a}_i = \frac{\mathbf{F}_i}{m_i}, \tag{4.23}$$

where m_i is the mass of the particle.

In molecular dynamics simulations it is often desirable to be able to control the temperature and pressure of the system. Several different methods exist to accomplish this. The work presented in the present thesis mostly employs the Nosé-Hoover thermostat and barostat, a method in which additional degrees of freedom are added to the system and coupled to the particle velocities and system size. The system can exchange energy with these additional degrees of freedom, which makes it possible to keep the temperature and pressure constant.

Apart from investigating the properties of a system at a finite temperature and pressure, molecular dynamics simulations can also be used in the process of finding the atomic configuration with the lowest energy. When minimizing the energy using an ordinary minimization algorithm, such as conjugate gradients, there is always a possibility that the algorithm will find a local minumum that does not correspond to the lowest possible energy. The system will then become stuck at this local minimum if it is separated from the real minimum by a high enough energy barrier. By performing a molecular dynamics simulation of the system at an elevated temperature, the energy barrier can be overcome and a larger number of states will be sampled.

The temperature can then be lowered to make the system approach a configuration corresponding to an energy minimum, hopefully the global minimum. This method has been applied in the search for the optimum grain boundary structure in both barium zirconate (Paper II) and graphene (Papers IV and V). Note that in the case of a grain boundary, the real global minimum in the system energy corresponds to the perfect crystal, whereas we are looking for the atomic configuration that gives the lowest energy provided that the grain boundary is still present.

Phonon wave packets

For the study of phonon scattering in Papers IV and V, a different approach was used. Instead of studying a system at equilibrium, we deliberately introduced a disturbance in the form of a phonon wave packet and studied how it scattered against the grain boundary. By calculating the kinetic energy after scattering in different regions of the supercell, and in different vibration modes, we could extract information about the scattering process.

In order to produce the required information about the scattering process, the wavepackets must have a well-defined wavenumber. Since it is necessary to use a finite simulation cell, the wavepacket must also be localized in the direction perpendicular to the grain boundary (the x direction). To accomplish this, we have used the method introduced by Schelling et al. [141, 142] and further developed by Kimmer et al. [143], in which the phonon modes of the perfect lattice are used as a basis set for constructing a localized wavepacket. The initial displacement and velocity of an atom i are calculated as

$$u_i = \text{Re} \sum_{\mathbf{k}} a_{\mathbf{k}} \varepsilon_{i\mathbf{k}} e^{\text{i}(\mathbf{k}\cdot\mathbf{R}_i - \omega(\mathbf{k})t)}, \qquad (4.24)$$

$$v_i = -\text{Re} \sum_{\mathbf{k}} \text{i}\omega(\mathbf{k}) a_{\mathbf{k}} \varepsilon_{i\mathbf{k}} e^{\text{i}(\mathbf{k}\cdot\mathbf{R}_i - \omega(\mathbf{k})t)} \qquad (4.25)$$

where $\mathbf{k} = k_x \hat{x} + k_y \hat{y}$ is a wavevector, $\mathbf{R}_i$ is the position of the atom, $\varepsilon_{i\mathbf{k}}$ is the polarization vector for wavevector $\mathbf{k}$ for the phonon branch under consideration and $\omega(\mathbf{k})$ is the angular frequency. The amplitudes $a_{\mathbf{k}}$ are given by

$$a_{\mathbf{k}} = A e^{-\eta^2 (k_x - k_{0x})^2} e^{-\text{i}\mathbf{k}\cdot\mathbf{R}_0}, \qquad (4.26)$$

where A is a constant determining the maximum amplitude and η is the width of the wavepacket in the x direction. This results in a wavepacket centered around the position $\mathbf{R}_0$ in real space and around a wavevector $\mathbf{k}_0 = k_{0x}\hat{x} + k_y\hat{y}$ in reciprocal space. Note that the wavepacket is only actually localized in x in real space, and infinite in the direction parallel to the grain boundary. This is necessary as periodic boundary conditions are applied in this direction.

After the scattering has taken place, the amplitude for each phonon branch and wavevector can be obtained from the displacement and velocity of the atoms according to

$$a_{\mathbf{k}} = \sum_i \varepsilon_{i\mathbf{k}}^* \left(u_i + \frac{\text{i}v_i}{\omega(\mathbf{k})} \right) e^{-\text{i}\mathbf{k}\cdot\mathbf{R}_i}, \qquad (4.27)$$

where $\varepsilon_{i\mathbf{k}}^*$ is the complex conjugate of the polarization vector. This makes it possible to obtain not only the total reflection and transmission at the boundary but also to observe any changes in the wavevector components, which is utilized in Paper V.

4.3 Continuum mechanical modeling

If the simulation supercell required to study a problem contains about 10^6 atoms or more, even simulation using interatomic model potentials can become too computationally demanding. In this case, it may be necessary to abandon the atomistic picture and model the material as continuous. Such a model may also contribute to the understanding of the studied phenomena as it can provide a simpler description. In this thesis, a continuum mechanical model has been developed for the phonon scattering at graphene grain boundaries. By finding a simple way to model the features of the grain boundary that are essential to scattering and solving the equations of motion for the system, the scattering results from the molecular dynamics simulations could be reproduced.

4.3.1 Equations of motion

In the continuum mechanical model, the graphene sheet is treated as a membrane characterized by a bending rigidity κ, the Lamé parameters λ and μ, and a two-dimensional density ρ. To find the equations of motions for displacements in such a membrane, we consider the Lagrangian of the system, which can be written

$$\mathcal{L} = \mathcal{T} - \mathcal{F}_b - \mathcal{F}_s, \tag{4.28}$$

Here, $\mathcal{T}$ is the kinetic energy which is given by

$$\mathcal{T} = \frac{\rho}{2}(\dot{u}^2 + \dot{v}^2 + \dot{w}^2), \tag{4.29}$$

where u and v are in-plane displacements in the x and y directions, and w is the out of plane displacement. The second term stands for the bending energy,

$$\mathcal{F}_b = \frac{\kappa}{2}|\nabla^2 w|^2, \tag{4.30}$$

and the third term represents the stretching energy,

$$\mathcal{F}_s = \frac{1}{2}[\sigma_{xx}\varepsilon_{xx} + 2\sigma_{xy}\varepsilon_{xy} + \sigma_{yy}\varepsilon_{yy}]. \tag{4.31}$$

Here, ε_{xx}, ε_{xy} and ε_{yy} are the components of the strain tensor, and σ_{xx}, σ_{xy} and σ_{yy} are the components of the stress tensor. The strain tensor components are given by [62]

$$\varepsilon_{xx} = \partial_x u + \frac{1}{2}(\partial_x w)^2 \tag{4.32}$$

$$\varepsilon_{xy} = \frac{1}{2}(\partial_x v + \partial_y u + \partial_x w \partial_y w) \tag{4.33}$$

$$\varepsilon_{yy} = \partial_y v + \frac{1}{2}(\partial_y w)^2. \tag{4.34}$$

These expressions are valid if the length scale of the displacement is much larger than the length scale of any underlying structure of the material. In the case of graphene, this means that the length scale of the displacements should be much larger than the lattice constant. According to Hooke's law, the stress tensor components are given by

$$\sigma_{xx} = (\lambda + 2\mu)\varepsilon_{xx} + \lambda\varepsilon_{xy} \tag{4.35}$$

$$\sigma_{xy} = 2\mu\varepsilon_{xy} \tag{4.36}$$

$$\sigma_{yy} = \lambda\varepsilon_{xy} + (\lambda + 2\mu)\varepsilon_{yy}. \tag{4.37}$$

The equations of motion for the displacements are then found to be

$$\rho\ddot{u} - \partial_x\sigma_{xx} - \partial_y\sigma_{xy} = F_x \tag{4.38}$$

$$\rho\ddot{v} - \partial_x\sigma_{xy} - \partial_y\sigma_{yy} = F_y \tag{4.39}$$

$$\rho\ddot{w} + \kappa\Delta^2 w - \partial_x[\sigma_{xx}\partial_x w + \sigma_{xy}\partial_y w] - \partial_y[\sigma_{xy}\partial_x w + \sigma_{yy}\partial_y w] = F_z, \tag{4.40}$$

where F_x, F_y and F_z are external forces. In our model, these forces are generally zero.

4.3.2 Modeling the grain boundary

In the molecular dynamics simulations, the structure of the grain boundaries could be described at the atomic level, and the resulting out-of-plane buckling determined as a consequence of the lattice defects. The continuum model, on the other hand, by definition does not include an atomic-level description of the defects at the boundary. However, it can be noted that according to the molecular dynamics results in Paper IV, the feature of the grain boundary that is relevant for scattering is the out-of-plane buckling. This buckling can be described by a static out-of-plane displacement of the form

$$w_0(x,y) = \chi e^{-x^2/2\eta^2}\left[1 + a\sin\left(\frac{2\pi my}{L_y}\right)\right], \tag{4.41}$$

where χ, η, a and m are constants that are determined through fitting to the grain boundary buckling seen in molecular dynamics simulations, and L_y is the periodicity of the grain boundary.

The introduction of an out-of-plane displacement will in general also result in in-plane displacements. For the one-dimensional model applied in Paper IV, the in-plane displacements could be obtained from Equation 4.38, whereas for the more complex two-dimensional model in Paper V they were obtained by fitting to stress tensor components obtained from the molecular dynamics simulations.

4.3.3 The finite difference method

Taking a closer look at Equations 4.38, 4.39 and 4.40, it is clear that obtaining an analytical solution would be quite difficult. Instead, the problem was treated numerically using finite difference methods. The displacements were thus evaluated at

discrete steps in time and space using an explicit scheme [144]. The most common finite difference approximation of the derivative of a function $f(x)$ is

$$\frac{df}{dx} \approx \frac{f(n+1) - f(n-1)}{2\Delta x}, \qquad (4.42)$$

where Δx is the discretization step size and n refers to a particular point where $x = n\Delta x$. Second and fourth derivatives can likewise be approximated as

$$\frac{d^2 f}{dx^2} \approx \frac{f(n+1) - 2f(n) + f(n-1)}{(\Delta x)^2} \qquad (4.43)$$

$$\frac{d^4 f}{dx^4} \approx \frac{1}{(\Delta x)^4}[f(n+2) - 4f(n+1) + 6f(n) - 4f(n-1) + f(n-2)], \qquad (4.44)$$

and for derivatives in two dimensions one obtains for example

$$\frac{d^2 f}{dxdy} \approx \frac{f(n+1,m+1) - f(n+1,m) - f(n,m+1) + f(n-1,m-1)}{4\Delta x \Delta y}, \qquad (4.45)$$

where Δy is the discretization step in the y direction. Discretizing Equations 4.38, 4.39 and 4.40 accordingly, we see that the second derivative with respect to time will contain the displacement at the next timestep. Solving for this term makes it possible to calculate the time evolution of the displacements. We can thus introduce a wavepacket equivalent to the ones used in the molecular dynamics simulations and study the way it scatters against the static out-of-plane displacement representing the grain boundary. The results can then be directly compared to the molecular dynamics results, which is an advantage of this method.

4.4 Summary

This chapter has given brief introductions to three computational methods: Density functional theory, with which the electron structure of a material can be determined, interatomic potential calculations, which do not yield the electron structure but still provide an atomistic description, and continuum mechanical modeling where the studied material is treated as a continuum. Each of these three models has its own advantages and disadvantages, and the choice of method for a specific problem must be made on the basis of the size of the systems to be modeled and the degree of accuracy required in the description of the material.

With the exception of the continuum mechanical model, I have not written the computer code required for these calculations myself. The density functional theory calculations have been performed using the Vienna *Ab-initio* Simulation Package, VASP, a density functional theory code that employs a plane-wave basis set [145, 146]. Molecular dynamics simulations of barium zirconate were performed using the DL_POLY program package [147], while the program package LAMMPS [148] was chosen for molecular dynamics simulations of graphene.

Chapter 5

Results and Conclusion: BaZrO$_3$

The aim of Papers I-III is to ascertain whether segregation of oxygen vacancies and protons can explain the low proton conductivity across grain boundaries in barium zirconate, as was discussed in Chapter 2. In all three papers, segregation energies have been determined using either density functional theory or model potential simulations. The segregation energies have then been used in thermodynamic space-charge models to obtain the potential barrier and defect concentration profiles in the space charge layers.

5.1   Grain boundary notation

The grain boundaries studied in Papers I-III are all tilt grain boundaries and have been labeled according to the Miller index of the grain boundary plane and the direction around which the grains are rotated. Thus, if the grain boundary plane is a (112) plane and the grains are rotated with respect to each other around the $[\bar{1}10]$ direction, the grain boundary is referred to as a $(112)[\bar{1}10]$ boundary. The construction of such a grain boundary is illustrated in Figure 5.1.

   In addition to the rotation, the grains may also be displaced with respect to one another parallel to the grain boundary plane. In Figure 5.1(b), it can be seen that the directions [111] and $[\bar{1}10]$ are parallel with the grain boundary plane for a $(112)[\bar{1}10]$ grain boundary. The grain boundary structure is periodic along these directions, with a period of $\sqrt{3}a_0$ in the [111] direction and $\sqrt{2}a_0$ in the $[\bar{1}10]$ direction, where a_0 is the lattice constant. The displacement of the grains is indicated in fractions of these grain boundary lattice periods, with the symmetric configuration in Figure 5.1(b) taken to be that of zero displacement. Thus, if the grains are displaced from the symmetric configuration by 2/3 lattice periods in the [111] direction the boundary is referred to as the $(112)[\bar{1}10](0,2/3)$ boundary. This is the configuration that can be seen in Figure 5.1(c).

[111]

[$\bar{1}$10]   [112]

(a)

[111]

[112]

[$\bar{1}$10]

(b)

[111]

[112]

[$\bar{1}$10]

(c)
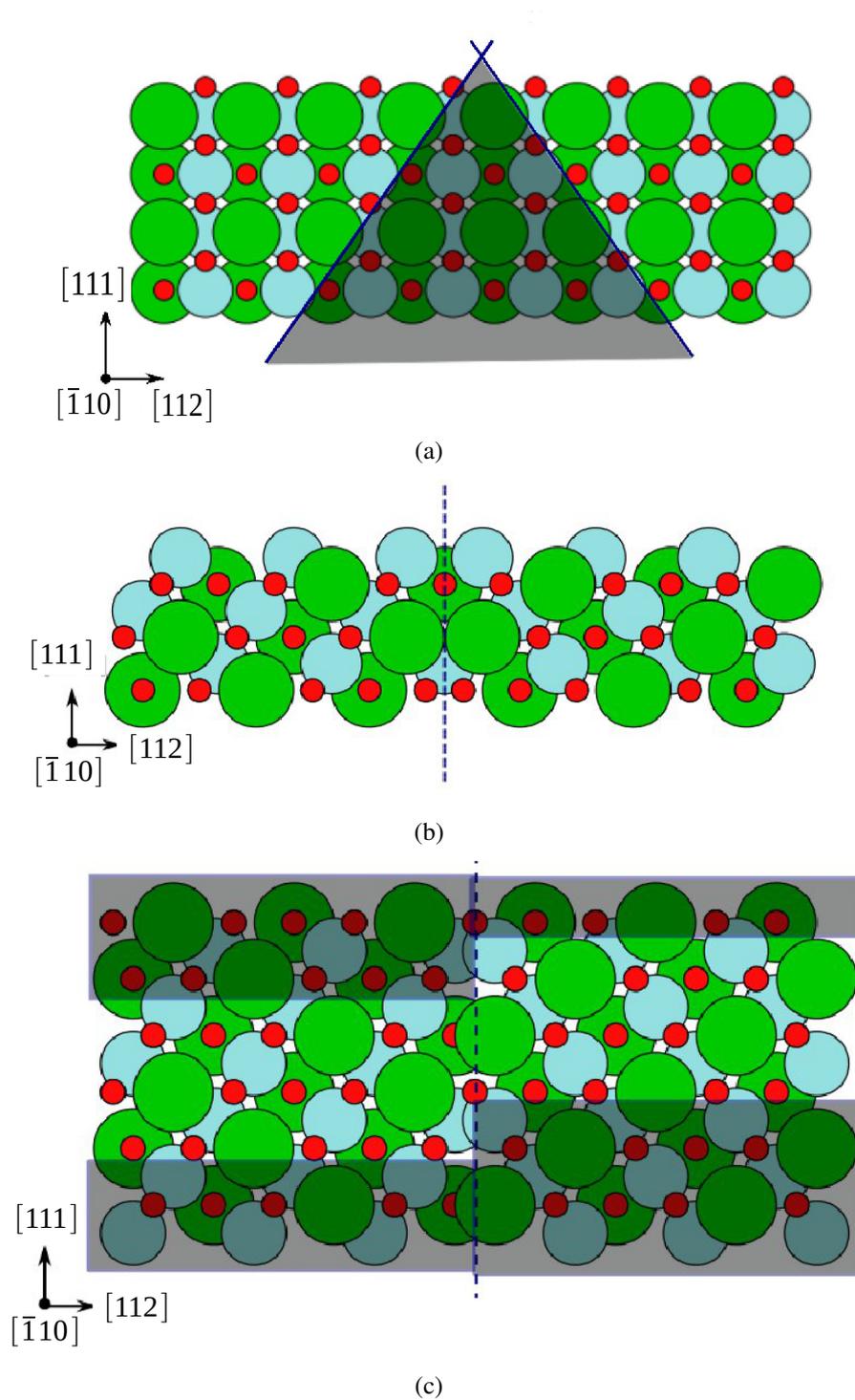
Figure 5.1: Creating the (112)[$\bar{1}$10] grain boundary. The block in 5.1(a) is cut perpendicular to the [112] and [1$\bar{1}$2] directions. The shaded area is removed. Tilting around the [$\bar{1}$10] direction produdes the symmetric configuration in 5.1(b). Displacement by 2/3 lattice periods in the [111] direction creates 5.1(c). Dashed lines indicate the grain boundary plane.
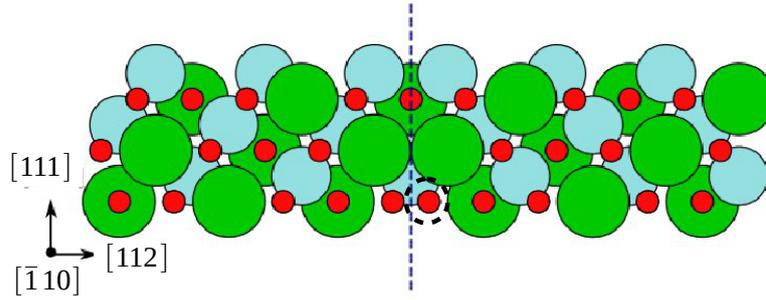
Figure 5.2: The $(112)[\bar{1}10](0,0)$ grain boundary with a dashed circle indicating the oxygen site with the most negative segregation energy.

5.2 Paper I

In Paper I, oxygen vacancy segregation to the $(112)[\bar{1}10](0,0)$ grain boundary was studied using density functional theory. The segregation energy ΔE_V of the vacancy is defined as the difference between the formation energy of a vacancy at the boundary, $E_{GB,V}^f$, and the formation energy of a vacancy in a reference state, $E_{REF,V}^f$, so that

$$\Delta E_V = E_{GB,V}^f - E_{REF,V}^f. \tag{5.1}$$

In Paper I the reference state is taken to be a vacancy in a supercell without grain boundary, while in the later papers the reference state is a vacancy as far away from the grain boundary as possible in the same supercell. According to this definition, a negative segregation energy signifies that the vacancy is more stable at the boundary than in bulk.

For the $(112)[\bar{1}10](0,0)$ grain boundary, the site with the most negative vacancy segregation energy was found to be situated next to the grain boundary layer, as is indicated in Figure 5.2. The segregation energy for this site was calculated to be -1.25 eV, substantially lower than the other sites near the grain boundary which were found to have segregation energies above -0.5 eV. It is probable that the strongly negative segregation energies next to the grain boundary plane are due to the oxygen-oxygen distances being considerably shorter than in bulk. It was also observed that on removal of an oxygen atom in the position indicated in Figure 5.2, the corresponding oxygen atom across the boundary relaxes into the middle of the grain boundary. This relaxation is accompanied by a substantial decrease in the energy of the system.

In the space charge model, the grain boundary sites with moderate segregation energies were neglected and only segregation to the site with the most negative segregation energy was considered. The vacancy concentration in the boundary core and the resulting potential barrier were calculated for both dry and hydrated conditions at temperatures between 300 and 1200 K. Under dry conditions, with no protons present, approximately 20 % of the oxygen sites in the core were found to be vacant at experimentally relevant temperatures (about 400-900 K). This resulted in an electrostatic barrier height of around 0.6 V. Hydrating the material lowers the

vacancy concentration in the core, particularly at low temperatures when the proton concentration in the grain interior is high. Even so, about 17 % of the sites in the core are vacant even at 300 K and the potential barrier is 0.33 V. At higher temperatures, around 600 K, the vacancy concentration in the core nearly reaches 20 % and the potential barrier is 0.45 V. A substantial potential barrier is thus generated even when the material is hydrated.

5.3 Paper II

In Paper II, an interatomic model potential is used to extend the investigation of oxygen vacancy segregation to a larger set of grain boundaries. The grain boundaries have the $[\bar{1}10]$ direction as tilt axis and a $(11i)$ plane as grain boundary plane, where $i = 1, 2...8$. With the exception of the $(111)[\bar{1}10]$ grain boundary, the model potential does not predict the symmetric grain boundary configuration to be the most stable but instead yields configurations where the grains are displaced with respect to one another. Two of the grain boundaries, the $(111)[\bar{1}10]$ and the $(112)[\bar{1}10](0,2/3)$, have grain boundary periods short enough that they can be studied with density functional theory. For these two boundaries, density functional theory and the model potential were found to yield similar grain boundary and vacancy segregation energies, indicating that the model potential is reliable. Oxygen vacancies were found to segregate to all eight considered grain boundaries, with segregation energies between -0.5 and -2.0 eV.

In contrast to the $[\bar{1}10](112)(0,0)$ grain boundary studied in Paper I, the larger boundaries were found to contain several different oxygen sites with substantially negative segregation energies. Oxygen sites at the same distance from the boundary plane were also found to have different segregation energies. To obtain the defect concentration as a function of distance from the boundary plane, as required in the space charge model, the grain boundary core was treated as a stack of layers containing oxygen sites with different segregation energies. The concentration at each site was calculated by assuming it to be in equilibrium with the grain interior, and the total vacancy concentration as a function of position was obtained as a sum over all sites in the layer. The calculated electrostatic barrier heights range from 0.2 to 0.8 V under dry conditions. Contrary to experimental results, neither increased total dopant concentration nor aggregation of dopants in the grain boundary region were found to affect the barrier heights. This is due to that not all low-energy sites in the grain boundary core are vacant, and the vacancy concentration in the core can therefore increase in response to the increased dopant concentration. The potential barrier thus remains relatively constant.

54

5.4 Paper III

In Paper III, the segregation energies of both protons and oxygen vacancies are calculated for the $(111)[\bar{1}10](0,0)$, $(112)[\bar{1}10](0,0)^*$ and $(210)[001](0,0)$ grain boundaries using density functional theory. Both defect types were found to segregate to all three grain boundaries. The vacancy segregation energy at the $(112)[\bar{1}10](0,0)$ grain boundary was found to be -1.5 eV, while the $(111)[\bar{1}10](0,0)$ and $(210)[001](0,0)$ boundaries yielded segregation energies of -0.54 and -0.47 eV, respectively. The proton segregation energies obtained were about -0.8 eV at all three grain boundaries.

In the space charge model, the grain boundary core was treated as a stack of layers and the different sites in each layer were considered separately, as in Paper II. Since both protons and vacancies segregate to the grain boundary, each oxygen site in the core has three possible states: Vacant, occupied by an oxygen ion, or occupied by a protonic defect in the form of a hydroxide ion. To obtain the concentrations of each defect type as a function of distance from the boundary plane, the probability for each site of being vacant or occupied by a protonic defect was calculated and the total concentration of each defect was obtained as a sum over the defect sites.

Under hydrated conditions and at temperatures below 700 K, protons were found to be more abundant than vacancies in all three grain boundary cores. At low temperatures the proton concentration was close to 30 % in all boundaries, generating potential barrier heights of about 0.6 V. The proton concentrations in all three boundaries were seen to decrease with increasing temperature, leading to a substantial decrease in the potential barrier height for the $(111)[\bar{1}10](0,0)$ and $(210)[001](0,0)$ boundaries. At the $(112)[\bar{1}10](0,0)$ boundary, however, the potential barrier remained above 0.5 V at all temperatures due to a substantial increase in the concentration of oxygen vacancies in the core at around 800 K.

The difference between the potential barriers of the three grain boundaries at high temperatures were found to be due to the differences in oxygen vacancy segregation energy. The smaller vacancy segregation energies of the $(111)[\bar{1}10](0,0)$ and $(210)[001](0,0)$ grain boundaries are not sufficient to maintain a high core charge in the absence of protons, while the stronger oxygen vacancy segregation at the $(112)[\bar{1}10](0,0)$ causes considerable segregation of vacancies and thus generates a potential barrier also under dry conditions. This indicates that segregation of protons can contribute substantially to the space charge effect, particularly at grain boundaries where protons segregate more strongly than oxygen vacancies.

---

*The oxygen vacancy segregation energies of the $(112)[\bar{1}10](0,0)$ grain boundary were recalculated using the PBE exchange-correlation functional, instead of PW91 which was used in Paper I.

5.5   Conclusion and Outlook

From the results of Paper I-III, it is clear that both protons and oxygen vacancies segregate to several grain boundaries in barium zirconate. The segregation is strong enough to generate a substantial positive core charge and electrostatic potential barriers with heights between 0.5 and 0.7 V at experimentally relevant temperatures, between 400 and 900 K. These barrier heights compare well with experimental data (see *e.g.* Refs. [20, 37, 38, 149]), indicating that the low grain boundary conductivity in barium zirconate can indeed be explained by space charge effects arising from segregation of protons and oxygen vacancies. However, the experimentally observed reduction of the barrier height following dopant segregation [39, 55] has not been reproduced by the present studies.

That the dopant concentration was found not to affect the electrostatic potential barrier is in all probability connected to one of the main issues remaining to be clarified, namely that of defect-defect interactions. The defect segregation energies reported here are intended to be valid for isolated, noninteracting defects, and the space charge models rely on the assumption that the defects only interact with each other electrostatically. However, according to the same space charge models the concentration of oxygen vacancies per site in the grain boundary core may be as high as 20 %, and in Paper III the proton concentration in the core reaches 30 % at low temperature. At these concentrations the defects may start to interact in ways not captured by the electrostatic potential in the space charge model, for example through the distortions they cause in the lattice, which would alter the segregation energies. It would therefore be of interest to study grain boundaries with multiple defects, especially if concentration dependent segregation energies could be obtained. An investigation of the interaction between an oxygen vacancy and a proton in a grain boundary has recently been conducted by Yang et al. [33], who found that the proton segregates to the boundary core also in the presence of an oxygen vacancy, but that the segregation energy is less negative at sites close to the vacancy. However, the study was focused on the activation energy for proton migration and did not further explore the relation between defect concentration and segregation energy.

It is likely that defect-defect interactions in the grain boundary core would decrease the magnitude of the negative segregation energies, making it less energetically favourable for defects to segregate. This effect could alter the results reported in Paper II with regard to the influence of dopant concentration. In the present model, the concentration of sites with negative segregation energy is high enough that the vacancy concentration in the core is only limited by electrostatic repulsion at realistic dopant concentrations. Vacancy-vacancy interactions may effectively reduce the number of available sites, thus lowering the maximum possible vacancy concentration in the core. When the maximum concentration of vacancies has been reached, a further increase in dopant concentration can be expected to cause the lowering of the potential barrier observed in experiments [39, 55]. Theoretical studies [56] that assume a lower concentration of sites with negative segregation energy in the grain boundary have found that the potential barrier height starts to decrease with

increasing dopant concentration once the sites with negative segregation energy are occupied by defects.

As experimental studies also suggest that the dopant atoms segregate to the grain boundary region during sintering, it is relevant to investigate the interaction between dopants, oxygen vacancies, and protons in the grain boundary. Previously, the stability of oxygen vacancies and yttrium dopants at the surfaces of barium zirconate and barium cerate has been studied [150], as well as the effect of zinc ions on proton transport [30]. However, the effects of dopant ions on the segregation energies of oxygen vacancies and protons at grain boundaries are largely unknown and would be an interesting subject of further study.

Chapter 6

Results and Conclusion: Graphene

In Chapter 3 of this thesis, the consequences of the two-dimensional nature of graphene in the contexts of phonons and grain boundaries were described. The papers summarized in the present chapter explore these topics further by investigating the scattering of flexural phonons against graphene grain boundaries. In both papers the scattering is studied using interatomic model potentials and molecular dynamics simulations. A continuum mechanical model of the system is also constructed.

6.1   Paper IV

The chief aim of Paper IV was to determine to what extent long-wavelength flexural phonons would be scattered by graphene grain boundaries. Three grain boundaries with tilt angles of 9.4°, 17.9° and 32.2° were chosen. The 9.4° and 17.9° grain boundaries both display out-of-plane buckling. For the 9.4° boundary, the height and width of the buckling are 0.6 and 1.7 nm, respectively, while for the 17.9° boundary the height of the buckling is 1.5 nm and the width is 5 nm. The 32.2° grain boundary was found to be flat. Compared to other studies of grain boundaries in graphene, the buckling found for the 9.4° and 17.9° boundaries is rather large. This may be attributed to variations in cell size and boundary conditions between the present and previous studies.

Once the boundary structure and buckling had been determined, phonon wave-packets with central wavevectors between 1 and 6 nm were introduced into the simulation supercells and allowed to scatter against the boundaries. Only normal incidence was considered. At the buckled boundaries, the scattering was found to be quite substantial. Transmission at the 9.4° boundary was found to range between 40 and 70 % of the total kinetic energy in the considered wavevector interval, while the transmission at the 17.9° boundary varied between 20 and 80 %. In contrast, more than 90 % of the kinetic energy was transmitted through the flat 32.2° grain boundary for all wavevectors. This clearly demonstrates that long-wavelength flexural phonons are scattered by grain boundaries that display out-of-plane buckling. Unexpectedly, some of the energy was found to be scattered into the in-plane longitudinal acoustic mode.
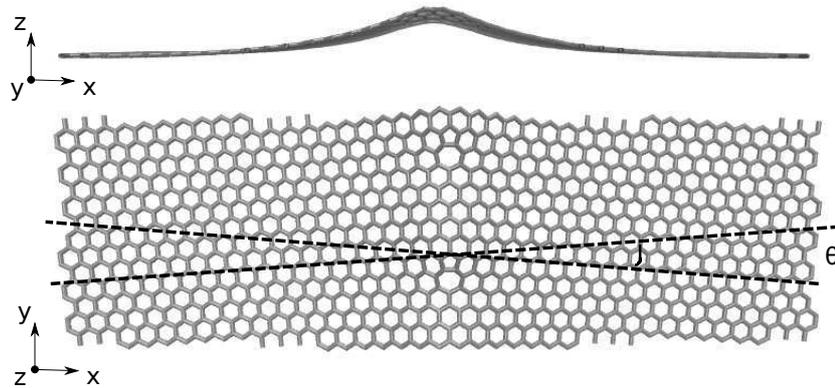
Figure 6.1: The 9.4° grain boundary, seen from the *y* direction (top) and the *z* direction (bottom). Figure from Paper V.

In order to obtain a better understanding of these results, a continuum mechanical model of the system was developed. Since only the flexural and longitudinal vibrational modes were found to be relevant, a one-dimensional continuum mechanical model was considered sufficient. As was described in Chapter 4, the grain boundary buckling was modeled as a static out-of-plane displacement. To model the 9.4° grain boundary, the static displacement was given the same height and width as the boundary buckling obtained in the molecular dynamics simulations. The model was found to reproduce the molecular dynamics transmission with reasonable accuracy, especially for the smallest wavenumbers. In contrast, modeling the 17.9° boundary using the buckling height and width from the molecular dynamics simulations did not produce a very good agreement for the transmission. However, reducing the width from 5 to 2 nm improved the agreement between the molecular dynamics simulations and the model considerably. The reason for this improvement is most likely that with the reduced width, the static displacement describes the curvature at the peak of the boundary buckling more accurately.

6.2 Paper V

In Paper V, the influence of angle of incidence on the scattering was investigated. In this study, only the buckled grain boundaries with misorientation angles of 9.4° and 17.9° were considered.

Substantial scattering was observed also for oblique incidence, with transmission ranging from 4 % to 65 % for the 9.4° boundary and reaching up to 80 % for the 17.9° boundary. The extremely low transmission of only 4 % was only seen for incidence angles near 35° and small total wavevector magnitudes. A less pronounced dip in transmission was also seen for the same angle but larger wavevector magnitude at the 9.4° boundary. In general, the transmission was found to increase
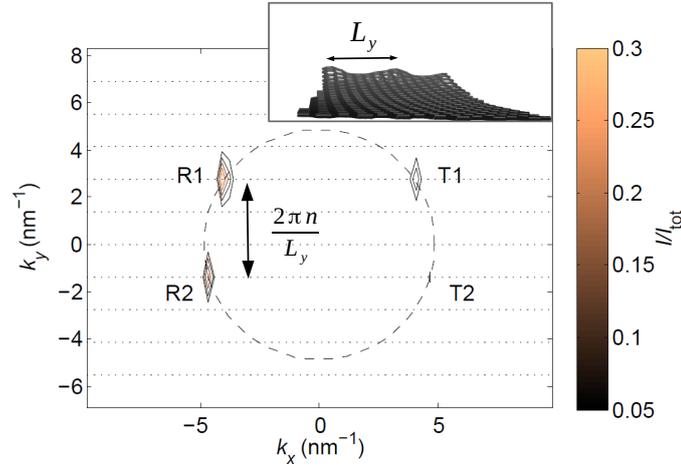
Figure 6.2: Illustration of diffraction at grain boundaries. The plot of the intensity as a function of k_x and k_y in reveals two transmitted pulses T1 and T2 and two reflected pulses R1 and R2. T1 has the same wavevector as the incoming pulse, and the difference in k_y between the incident and scattered pulses is $2\pi n/L_y$ ($n = 0, 1$). The dotted lines mark the values of k_y allowed by the boundary conditions, while the dashed circle indicates wavevectors of the same magnitude as that of the incident pulse. In the inset, the height variation of the grain boundary buckling is shown and the period L_y is indicated (the grain boundary is seen from the x direction).

with decreasing incidence angle.

In contrast to the case of normal incidence, only negligible in-plane vibrations were seen in this study. However, several pulses with different wavevectors could be observed after scattering. The difference in wavevector between the incident and scattered pulses was found to be connected to the grain boundary periodicity. Let the direction perpendicular to the grain boundary be x and the direction parallel to the grain boundary be y, as in Figure 6.1. Denoting the y component of the wavevector of the incident pulse as k_y^{in}, the x component as k_x^{in}, and the magnitude as k^{in}, the wavevector components of the scattered pulses were given by

$$k_y = k_y^{\text{in}} + \frac{2\pi n}{L_y}$$

(6.1)

$$k_x = \sqrt{(k^{\text{in}})^2 - k_y^2},$$

where n is an integer and L_y is the grain boundary period (see Figure 6.2). Thus, it is clear that the grain boundaries act as diffraction gratings, in all probability due to the periodic variation in buckling height caused by the periodic distribution of pentagon-heptagon defects along the boundary. Both the diffraction and the dependence of the total transmission on the incidence angle were well reproduced by a two-dimensional continuum mechanical model based on the same principles as the one-dimensional model used in Paper IV.

6.3 Conclusion and Outlook

In Papers IV and V, it has been shown that buckled grain boundaries in graphene cause significant scattering of long-wavelength flexural phonons. For normal incidence some of the energy is scattered into the in-plane longitudinal vibration mode, while for oblique incidence the grain boundary is observed to act as a diffraction grating. The scattering can be fairly well described using a continuum mechanical model where the grain boundary is included as a static out-of-plane displacement corresponding to the boundary buckling.

Although the results presented here provide an improved understanding of the interaction between flexural phonons and grain boundaries, the total effect of buckled grain boundaries on thermal conductivity is not clear. Previous studies aimed at calculating the grain boundary thermal conductivity have typically not considered the grain boundary buckling [98–101, 151, 152], which according to the present study is likely to be very significant. It may thus be worthwhile to attempt to obtain the total thermal conductivity of a buckled grain boundary, or perhaps even of a set of grain boundaries with different buckling heights and widths. This could be done either using nonequilibrium molecular dynamics or Green's function methods, or by extending the present study to smaller wavenumbers and in-plane phonon branches.

The flexural mode in graphene is also relevant to the understanding of graphene nanoresonator systems, and it might thus be interesting to apply the present results to nanoresonators containing grain boundaries. The continuum mechanical model could be of use in this context as it is capable of describing systems of micrometer size, something that is still very demanding to do using atomistic simulations.

6.3.1 Adsorption

In Chapter 3, it was mentioned that graphene grain boundaries are more reactive than pristine graphene. It was also argued that metals may adsorb more strongly to the grain boundaries, a possibility that merits further attention due to the potential applications in *e.g.* catalysis and sensing. However, metal adsoption is commonly studied using first-principles methods that give an exact description of the atom-atom interaction, while simulations of buckled grain boundaries often require simulation supercells too large for first principles simulations. To study metal adsorption at grain boundaries it would thus be necessary to find an interatomic potential that describes the metal-carbon interaction with sufficient accuracy.

In the search for an adequate model potential we have evaluated the two most commonly used potential types for the carbon-metal interaction, the Lennard-Jones pair potential and a Tersoff-Brenner bond-order potential. For the Lennard-Jones potential parameters describing the interaction of carbon and gold were chosen, while the bond-order potential is adapted to the interaction between carbon and platinum [136]. Unfortunately, neither potential was found to be entirely adequate.

The potentials were evaluated through calculations of the adsorption energies of single atoms on pristine graphene and on a buckled graphene grain boundary.

For pristine graphene the adsorption energy was compared to density functional theory results available in the literature. Both potentials were found to give approximately the right adsorption energy at the most favourable adsorption site, but the Lennard-Jones potential predicts the wrong adsorption site as the most energetically favourable. The bond-order potential, on the other hand, predicts substantially weaker adsorption at the other adsorption sites compared to density functional theory [153]. This would for example affect any study involving diffusion of adsorbates.

For the adsorption at the grain boundary no first-principles results exist, but there are studies that suggest increased adsorption strength for gold and platinum on individual pentagon or heptagon defects [93], as well as on a curved graphene surface or a carbon nanotube [154, 155]. This indicates that stronger adsorption should be observed at the grain boundary, as it contains defects and displays buckling. The Lennard-Jones potential failed to reproduce this trend, predicting only slightly stronger adsorption energies at the buckled grain boundary. In contrast, the bond-order potential predicted the adsorption at the grain boundary to be stronger than on pristine graphene by about 0.8 eV, with especially strong adsorption at sites where the graphene displayed a strong curvature [153]. Despite this relative success, it is clear that better model potentials are required for studies of metal adsorption on graphene with grain boundaries. In particular, a potential modeling the interaction between gold adsorbates and graphene would be a useful contribution to the field.

Acknowledgements

My Ph.D. project was originally envisioned as a collaboration between two groups, that of Materials and Surface Theory and that of Condensed Matter Theory. Although the project aim has shifted over time, this still means that I have had the opportunity to work in both groups. I have also had two supervisors, Göran Wahnström and Andreas Isacsson. I wish to express my gratitude to them both for their patient guidance and sound advice. I would also like to thank my assistant supervisor Jari Kinaret.

My present and former colleagues in both research groups have also had an impact on my work. In particular I wish to acknowledge the contributions of Joakim Nyman, who first taught me density functional theory, and Anders Lindman, whom I have worked with on the barium zirconate project. Thanks also to Mattias Slabanja and his old colleagues at the Chalmers Centre for Computational Science and Engineering, C3SE.

Research is fascinating, but sometimes one has to take a break. I would therefore like to thank all my friends, who have reminded me of this fact from time to time. Last but not least, I would like to thank my parents and my brother for their encouragement and unfailing support.

Bibliography

[1] M. P. Marder, *Condensed Matter Physics* (Wiley-Interscience, New York, USA, 2000).

[2] J. Maier, *Physical Chemistry of Ionic Materials* (John Wiley and Sons Ltd., Chichester, England, 2004).

[3] P. E. J. Flewitt and R. K. Wild, *Grain Boundaries: Their Microstructure and Chemistry* (John Wiley and sons, Chichester, England, 2001).

[4] A. B. Stambouli and E. Traversa, *Fuel cells, an alternative to standard sources of energy*, Renewable and Sustainable Energy Reviews **6**, 297 (2002).

[5] L. Carrette, K. A. Friedrich, and U. Stimming, *Fuel Cells: Principles, Types, Fuels, and Applications*, ChemPhysChem **1**, 162 (2000).

[6] G. Crabtree, M. S. Dresselhaus, and M. V. Buchanan, *The hydrogen economy*, Physics Today **57**, 39 (2004).

[7] M. Momirlan and T. Veziroglu, *The properties of hydrogen as fuel tomorrow in sustainable energy system for a cleaner planet*, International Journal of Hydrogen Energy **30**, 795 (2005).

[8] S. M. Haile, *Fuel cell materials and components*, Acta Materialia **51**, 5981 (2003), the Golden Jubilee Issue. Selected topics in Materials Science and Engineering: Past, Present and Future.

[9] L. Malavasi, C. A. J. Fisher, and M. S. Islam, *Oxide-ion and proton conducting electrolyte materials for clean energy applications: structural and mechanistic features*, Chemical Society Reviews **39**, 4370 (2010).

[10] H. Iwahara, T. Esaka, H. Uchida, and N. Maeda, *Proton conduction in sintered oxides and its application to steam electrolysis for hydrogen production*, Solid State Ionics **3-4**, 359 (1981).

[11] H. Iwahara, H. Uchida, and S. Tanaka, *High temperature type proton conductor based on $SrCeO_3$ and its application to solid electrolyte fuel cells*, Solid State Ionics **9-10**, 1021 (1983).

[12] H. Iwahara, *Proton Conduction in Sintered Oxides Based on BaCeO$_3$*, Journal of the Electrochemical Society **135**, 529 (1988).

[13] H. Iwahara *et al.*, *Protonic conduction in calcium, strontium and barium zirconates*, Solid State Ionics **61**, 65 (1993).

[14] E. Fabbri, D. Pergolesi, and E. Traversa, *Materials challenges toward proton-conducting oxide fuel cells: a critical review*, Chemical Society Reviews **39**, 4355 (2010).

[15] E. Fabbri, L. Bi, D. Pergolesi, and E. Traversa, *Towards the Next Generation of Solid Oxide Fuel Cells Operating Below 600 °C with Chemically Stable Proton Conducting Electrolytes*, Advanced Materials **24**, 195 (2012).

[16] K. D. Kreuer, *Proton-Conducting Oxides*, Annual Review of Materials Research **33**, 333 (2003).

[17] H. G. Bohn and T. Shober, *Electrical Conductivity of the High-Temperature Proton Conductor BaZr$_{0.9}$Y$_{0.1}$O$_{2.95}$*, Journal of the American Ceramic Society **83**, 768 (2000).

[18] P. Babilo, T. Uda, and S. M. Haile, *Processing of Yttrium-Doped Barium Zirconate for High Proton Conductivity*, Journal of Materials Research **22**, 1322 (2007).

[19] F. Iguchi *et al.*, *The relationship between chemical composition distributions and specific grain boundary conductivity in Y-doped BaZrO$_3$ proton conductors*, Solid State Ionics **180**, 563 (2009).

[20] F. Iguchi, N. Sata, and H. Yugami, *Proton transport properties at the grain boundary of barium zirconate based proton conductors for intermediate temperature operating SOFC*, Journal of Materials Chemistry **20**, 6265 (2010).

[21] P. I. Dahl *et al.*, *Microstructural characterization and electrical properties of spray pyrolyzed conventionally sintered or hot-pressed BaZrO3 and BaZr0.9Y0.1O3*, Solid State Ionics **182**, 32 (2011).

[22] S. P. S. Badwal, *Grain boundary resistivity in zirconia-based materials: effects of sintering temperatures and impurities*, Solid State Ionics **76**, 67 (1995).

[23] M. Shirpour, R. Merkle, C. T. Lin, and J. Maier, *Nonlinear electrical grain boundary properties in proton conducting Y-BaZrO$_3$ supporting the space charge depletion model*, Physical Chemistry Chemical Physics **14**, 730 (2012).

[24] A. Lindman, Licentiate thesis, Chalmers University of Technology, 2015.

[25] E. Fabbri, A. Magraso, and D. Pergolesi, *Low-temperature solid-oxide fuel cells based on proton-conducting electrolytes*, MRS Bulletin **39**, 792 (2014).

[26] S. Ricote *et al.*, *Effects of the fabrication process on the grain boundary resistance in $BaZr_{0.9}Y_{0.1}O_{3-\delta}$*, Journal of Materials Chemistry A **2**, 16107 (2014).

[27] R. B. Cervera *et al.*, *Nanorgrained Sc-doped $BaZrO_3$ as a proton conducting solid electrolyte for intermediate temperature solid oxide fuel cells (IT-SOFCs)*, Solid State Ionics **264**, 1 (2014).

[28] T. Sugimoto and T. Hashimoto, *Structural phase relationship, sintering behaviour and conducting property of $Ba_{1-x}Sr_xZr_{0.9}Y_{0.1}O_{3-\delta}$*, Solid State Ionics **264**, 17 (2014).

[29] W. Sun *et al.*, *An Easily Sintered, Chemically Stable, Barium Zirconate-Based Proton Conductor for High-Performance Proton-Conducting Solid Oxide Fuel Cells*, Advanced Functional Materials **24**, 5695 (2014).

[30] D.-H. Kim, B.-K. Kim, and Y.-C. Kim, *Effect of zinc oxide as a sintering aid on proton migration across $\Sigma5$ (310)/[001] tilt grain boundary of barium zirconate*, Journal of Electroceramics **30**, 19 (2013).

[31] N. Kitamura *et al.*, *Proton Distribution and Dynamics in Y- and Zn-Doped $BaZrO_3$*, The Journal of Physical Chemistry C **118**, 18846 (2014).

[32] D. Pergolesi *et al.*, *High proton conduction in grain-boundary-free yttrium-doped barium zirconate films grown by pulsed laser deposition*, Nature Materials **9**, 846 (2010).

[33] J.-H. Yang, D.-H. Kim, B.-K. Kim, and Y.-C. Kim, *High activation energy for proton migration at $\Sigma3(111)/[1\bar{1}0]$ tilt grain boundary in barium zirconate*, Solid State Ionics **252**, 126 (2013).

[34] X. Guo and R. Waser, *Electrical properties of the grain boundaries of oxygen ion conductors: Acceptor-doped zirconia and ceria*, Progress in Materials Science **51**, 151 (2006).

[35] R. A. De Souza, *The formation of equilibrium space-charge zones at grain boundaries in the perovskite oxide $SrTiO_3$*, Physical Chemistry Chemical Physics **11**, 9939 (2009).

[36] F. Iguchi, C.-T. Chen, H. Yugami, and S. Kim, *Direct evidence of potential barriers at grain boundaries in Y-doped $BaZrO_3$ from dc-bias dependence measurements*, Journal of Materials Chemistry **21**, 16517 (2011).

[37] C. Kjølseth *et al.*, *Space-charge theory applied to the grain boundary impedance of proton conducting $BaZr_{0.9}Y_{0.1}O_{3-\delta}$*, Solid State Ionics **181**, 268 (2010).

[38] C.-T. Chen, C. E. Danel, and S. Kim, *On the origin of the blocking effect of grain-boundaries on proton transport in yttrium-doped barium zirconate*, Journal of Materials Chemistry **21**, 5435 (2011).

[39] M. Shirpour *et al.*, *Dopant Segregation and Space Charge Effects in Proton-Conducting BaZrO3 Perovskites*, The Journal of Physical Chemistry C **116**, 2435 (2012).

[40] M. Shirpour, R. Merkle, and J. Maier, *Evidence for space charge effects in Y-doped BaZrO3 from reduction experiments*, Solid State Ionics **216**, 1 (2012).

[41] K. Nomura and H. Kageyama, *Transport properties of Ba(Zr$_{0.8}$Y$_{0.2}$)O$_{3-\delta}$ perovskite*, Solid State Ionics **178**, 661 (2007).

[42] K. D. Kreuer, *Proton Conductivity: Materials and Applications*, Chemistry of Materials **8**, 610 (1996).

[43] W. Münch, K.-D. Kreuer, G. Seifert, and J. Maier, *Proton diffusion in perovskites: comparison between BaCeO3, BaZrO3, SrTiO3, and CaTiO3 using quantum molecular dynamics*, Solid State Ionics **136-137**, 183 (2000).

[44] K. D. Kreuer, in *Perovskite Oxide for Solid Oxide Fuel Cells*, edited by T. Ishihara (Springer US, Boston, MA, 2009), pp. 261–272.

[45] T. Norby, in *Perovskite Oxide for Solid Oxide Fuel Cells*, edited by T. Ishihara (Springer US, Boston, MA, 2009), pp. 217–241.

[46] K. D. Kreuer, *Aspects of the formation and mobility of protonic charge carriers and the stability of perovskite-type oxides*, Solid State Ionics **125**, 285 (1999).

[47] M. E. Björketun, P. G. Sundell, and G. Wahnström, *Structure and thermodynamic stability of hydrogen interstitials in BaZrO3 perovskite oxide from density functional calculations*, Faraday Discussions **134**, 247 (2007).

[48] M. E. Björketun, P. G. Sundell, and G. Wahnström, *The effect of acceptor dopants on the proton mobility in BaZrO3: A density functional study*, Physical Review B **76**, 054307 (2007).

[49] M. S. Islam, P. R. Slater, J. R. Tolchard, and T. Dinges, *Doping and defect association in AZrO3 (A=Ca, Ba) and LaMO3 (M=Sc, Ga) perovskite-type ionic conductors*, Dalton Transactions 3061 (2004).

[50] S. J. Stokes and M. S. Islam, *Defect chemistry and proton-dopant association in BaZrO3 and BaPrO3*, Journal of Materials Chemistry **20**, 6258 (2010).

[51] M. Yoshino *et al.*, *Local Electronic Structure and Protonic Conductivity in Perovskite-Type Oxide, SrZrO3*, Materials Transactions **46**, 1131 (2005).

[52] Y. Yamazaki *et al.*, *Proton trapping in yttrium-doped barium zirconate*, Nature Materials **12**, 647 (2013).

[53] J. A. Kilner, *Fast oxygen transport in acceptor doped oxides*, Solid State Ionics **129**, 13 (2000).

[54] H. Mehrer, *Diffusion in Solids* (Springer, Berlin, 2007).

[55] M. Shirpour *et al.*, *High spatially resolved cation concentration profile at the grain boundaries of Sc-doped BaZrO$_3$*, Solid State Ionics **262**, 860 (2014).

[56] R. A. De Souza, Z. A. Munir, S. Kim, and M. Martin, *Defect chemistry of grain boundaries in proton-conducting solid oxides*, Solid State Ionics **196**, 1 (2011).

[57] A. K. Geim and K. S. Novoselov, *The rise of graphene*, Nature Materials **6**, 183 (2007).

[58] K. S. Novoselov *et al.*, *A roadmap for graphene*, Nature **490**, 192 (2012).

[59] D. Akinwande, N. Petrone, and J. Hone, *Two-dimensional flexible nanoelectronics*, Nature Communications **5**, 5678 (2014).

[60] A. C. Ferrari *et al.*, *Science and technology roadmap for graphene, related two-dimensional crystals, and hybrid systems*, Nanoscale **7**, 4598 (2015).

[61] S. Hu *et al.*, *Proton transport through one-atom-thick crystals*, Nature **516**, 227 (2014).

[62] L. D. Landau and E. M. Lifshitz, *Theory of Elasticity*, 3:rd ed. (Elsevier, Oxford, Great Britain, 1986).

[63] L. Lindsay *et al.*, *Phonon thermal transport in strained and unstrained graphene from first principles*, Physical Review B **89**, 155426 (2014).

[64] L. Lindsay, D. A. Broido, and N. Mingo, *Flexural phonons and thermal transport in graphene*, Physical Review B **82**, 115427 (2010).

[65] N. Mounet and N. Marzari, *First-principles determination of the structural, vibrational and thermodynamic properties of diamond, graphite, and derivatives*, Physical Review B **71**, 205214 (2005).

[66] P. L. de Andres, F. Guinea, and M. I. Katsnelson, *Bending modes, anharmonic effects, and thermal expansion coefficient in single-layer and multi-layer graphene*, Physical Review B **86**, 144103 (2012).

[67] D. Yoon, Y.-W. Son, and H. Cheong, *Negative Thermal Expansion Coefficient of Graphene Measured by Raman Spectroscopy*, Nano Letters **11**, 3227 (2011).

[68] A. A. Balandin, *Thermal properties of graphene and nanostructured carbon materials*, Nature Materials **10**, 569 (2011).

[69] S. Ghosh *et al.*, *Extremely high thermal conductivity of graphene: Prospects for thermal management applications in nanoelectronic circuits*, Applied Physics Letters **92**, 151911 (2008).

[70] S. Yigen *et al.*, *Electronic thermal conductivity measurements in intrinsic graphene*, Physical Review B **87**, 241411 (2013).

[71] E. Pop, V. Varshney, and A. K. Roy, *Thermal properties of graphene: Fundamentals and applications*, MRS Bulletin **37**, 1273 (2012).

[72] D. L. Nika, E. P. Pokatilov, A. S. Askerov, and A. A. Balandin, *Phonon thermal conduction in graphene: Role of Umklapp and edge roughness scattering*, Physical Review B **79**, 155413 (2009).

[73] D. L. Nika, S. Ghosh, E. P. Pokatilov, and A. A. Balandin, *Lattice thermal conductivity of graphene flakes: Comparison with bulk graphite*, Applied Physics Letters **94**, 203103 (2009).

[74] D. Singh, J. Y. Murthy, and T. S. Fisher, *On the accuracy of classical and long wavelength approximations for phonon transport in graphene*, Journal of Applied Physics **110**, 113510 (2011).

[75] D. Singh, J. Y. Murthy, and T. S. Fisher, *Spectral phonon conduction and dominant scattering pathways in graphene*, Journal of Applied Physics **110**, 094312 (2011).

[76] J. H. Seol *et al.*, *Two-Dimensional Phonon Transport in Supported Graphene*, Science **328**, 213 (2010).

[77] Z. Wang *et al.*, *Thermal Transport in Suspended and Supported Few-Layer Graphene*, Nano Letters **11**, 113 (2011).

[78] X. Xu *et al.*, *Length-dependent thermal conductivity in suspended single-layer graphene*, Nature Communications **5**, 3689 (2014).

[79] G. Fugallo *et al.*, *Thermal Conductivity of Graphene and Graphite: Collective Excitations and Mean Free Paths*, Nano Letters **14**, 6109 (2014).

[80] G. Barbarino, C. Melis, and L. Colombo, *Intrinsic thermal conductivity in monolayer graphene is ultimately upper limited: A direct estimation by atomistic simulation*, Physical Review B **91**, 035416 (2015).

[81] P. Y. Huang *et al.*, *Grains and grain boundaries in single-layer graphene atomic patchwork quilts*, Nature **469**, 389 (2011).

[82] O. V. Yazyev and Y. P. Chen, *Polycrystalline graphene and other two-dimensional materials*, Nature Nanotechnology **9**, 755 (2014).

[83] K. Kim *et al.*, *Grain Boundary Mapping in Polycrystalline Graphene*, ACS Nano **5**, 2142 (2011).

[84] J. M. Carlsson, L. M. Ghiringhelli, and A. Fasolino, *Theory and hierarchical calculations of the structure and energetics of [0001] tilt grain boundaries in graphene*, Physical Review B **84**, 165423 (2011).

[85] T.-H. Liu, G. Gajewski, C.-W. Pao, and C.-C. Chang, *Structure, energy, and structural transformations of graphene grain boundaries from atomistic simulations*, Carbon **49**, 2306 (2011).

[86] O. V. Yazyev and S. G. Louie, *Topological defects in graphene: Dislocations and grain boundaries*, Physical Review B **81**, 195420 (2010).

[87] C. Lee, X. Wei, J. W. Kysar, and J. Hone, *Measurement of the Elastic Properties and Intrinsic Strength of Monolayer Graphene*, Science **321**, 385 (2008).

[88] O. Lehtinen, S. Kurasch, A. V. Krasheninnikov, and U. Kaiser, *Atomic scale study of the life cycle of a dislocation in graphene from birth to annihilation*, Nature Communications **4**, 2089 (2013).

[89] J. H. Warner *et al.*, *Dislocation-Driven Deformations in Graphene*, Science **337**, 209 (2012).

[90] J. Coraux, A. T. N'Diaye, C. Busse, and T. Michely, *Structural coherency of graphene on Ir(111)*, Nano Letters **8**, 565 (2008).

[91] G.-H. Lee *et al.*, *High-Strength Chemical-Vapor-Deposited Graphene and Grain Boundaries*, Science **340**, 1073 (2013).

[92] A. W. Cummings *et al.*, *Charge Transport in Polycrystalline Graphene: Challenges and opportunities*, Advanced Materials **26**, 5079 (2014).

[93] Y. Okamoto, *Density-functional calculations of icosahedral M_{13} (M=Pt and Au) clusters on graphene sheets and flakes*, Chemical Physics Letters **420**, 382 (2006).

[94] Q. Zhou *et al.*, *Electronic and magnetic properties of transition-metal atoms absorbed on Stone-Wales defected graphene sheet: A theory study*, Computational Materials Science **81**, 348 (2014).

[95] Q. Wang, F. Wang, J. Shang, and Y. Zhou, *An ab initio study of the interaction between an iron atom and graphene containing a single Stone-Wales defect*, Journal of Physics: Condensed Matter **21**, 485506 (2009).

[96] T. Zhang, L. Zhu, S. Yuan, and J. Wang, *Structural and Magnetic Properties of 3d Transition-Metal-Atom Adsorption on Perfect and Defective Graphene: A Density Functional Theory Study*, ChemPhysChem. **14**, 3483 (2013).

[97] L.-J. Zhou, Z. F. Hou, and L.-M. Wu, *First-principles study of lithium adsorption and diffusion on graphene with point defects*, Journal of Physical Chemistry C **116**, 21780 (2012).

[98] A. Cao and J. Qu, *Kapitza conductance of symmetric tilt grain boundaries in graphene*, Journal of Applied Physics **111**, 053529 (2012).

[99] A. Bagri, S.-P. Kim, R. S. Ruoff, and V. B. Shenoy, *Thermal transport across twin grain boundaries in polycrystalline graphene from nonequilibrium molecular dynamics simulations*, Nano Letters **11**, 3917 (2011).

[100] Y. Lu and J. Guo, *Thermal transport in grain boundary of graphene by non-equilibrium Green's function approach*, Applied Physics Letters **101**, 043112 (2012).

[101] A. Y. Serov, Z.-Y. Ong, and E. Pop, *Effect of grain boundaries on thermal transport in graphene*, Applied Physics Letters **102**, 033104 (2013).

[102] T.-H. Liu, S.-C. Lee, C.-W. Pao, and C.-C. Chang, *Anomalous thermal transport along the grain boundaries of bicrystalline graphene nanoribbons from atomistic simulations*, Carbon **73**, 432 (2014).

[103] X. Li, K. Maute, M. L. Dunn, and R. Yang, *Strain effects on the thermal conductivity of nanostructures*, Physical Review B **81**, 245318 (2010).

[104] J. Kohanoff, *Electronic Structure Calculations for Solids and Molecules: Theory and Computational Methods* (Cambridge University Press, Cambridge, 2006).

[105] M. Born and R. Oppenheimer, *Zur Quantentheorie der Molekeln*, Annalen der Physik **389**, 457 (1927).

[106] P. Hohenberg and W. Kohn, *Inhomogeneous Electron Gas*, Physical Review **136**, B864 (1964).

[107] W. Kohn, *Nobel Lecture: Electronic structure of matter - wave functions and density functionals*, Reviews of Modern Physics **71**, 1253 (1999).

[108] W. Kohn and L. J. Sham, *Self-Consistent Equations Including Exchange and Correlation Effects*, Physical Review **140**, A1133 (1965).

[109] D. M. Ceperly and B. J. Alder, *Ground State of the Electron Gas by a Stochastic Method*, Physical Review Letters **45**, 566 (1980).

[110] R. Jones and O. Gunnarson, *The density functional formalism, its applications and prospects*, Reviews of Modern Physics **61**, 689 (1989).

[111] J. P. Perdew, K. Burke, and M. Ernzerhof, *Generalized Gradient Approximation Made Simple*, Physical Review Letters **77**, 3865 (1996).

[112] F. Bloch, *Über die Quantenmechanik der Elektronen in Kristallgittern*, Zeitshrift für Physik **52**, 555 (1929).

[113] R. M. Martin, *Electronic Structure: Basic Theory and Practical Methods* (Cambridge University Press, Cambridge, 2004).

[114] R. P. Feynman, *Forces in Molecules*, Physical Review **56**, 340 (1939).

[115] Y. Mishin, M. R. Soerensen, and A. F. Voter, *Calculation of point-defect entropy in metals*, Philosophical Magazine A **81**, 2591 (2001).

[116] M. Leslie and M. J. Gillan, *The energy and elastic dipole tensor of defects in ionic crystals calculated by the supercell method*, Journal of Physics C: Solid State Physics **18**, 973 (1985).

[117] G. Makov and M. C. Payne, *Periodic boundary conditions in ab initio calculations*, Physical Review B **51**, 4014 (1995).

[118] L. Kantorovich, *Elimination of the long-range dipole interaction in calculations with periodic boundary conditions*, Physical Review B **60**, 15476 (1999).

[119] H. Nozaki and S. Itoh, *Energy correction for isolated impurities under periodic boundary conditions*, Physical Review E **62**, 1390 (2000).

[120] P. Schultz, *Local electrostatic moments and periodic boundary conditions*, Physical Review B **60**, 1551 (1999).

[121] I. Dabo, B. Kozinsky, N. E. Singh-Miller, and N. Marzari, *Electrostatics in periodic boundary conditions and real-space corrections*, Physical Review B **77**, 115139 (2008).

[122] N. D. M. Hine, K. Frensch, W. M. C. Foulkes, and M. W. Finnis, *Supercell size scaling of density functional theory formation energies of charged defects*, Physical Review B **79**, 024112 (2009).

[123] C. Freysoldt, J. Neugebauer, and C. G. Van de Walle, *Fully Ab Initio Finite-Size Corrections for Charged-Defect Supercell Calculations*, Physical Review Letters **102**, 016402 (2009).

[124] C. Freysoldt, J. Neugebauer, and C. G. Van der Walle, *Electrostatic interactions between charged defects in supercells*, Physica Status Solidi B **248**, 1067 (2011).

[125] Y. Kumagai and F. Oba, *Electrostatics-based finite-size corrections for first-principles point defect calculations*, Physical Review B **89**, 195205 (2014).

[126] C. W. M. Castleton, A. Höglund, and S. Mirbt, *Density functional theory calculations of defect energies using supercells*, Modelling and Simulation in Materials Science and Engineering **17**, 084003 (2009).

[127] R. M. Nieminen, *Issues in first-principles calculations for defects in semiconductors and oxides*, Modelling and Simulation in Materials Science and Engineering **17**, 084001 (2009).

[128] R. A. Buckingham, *The Classical Equation of State of Gaseous Helium, Neon and Argon*, Proceedings of the Royal Society of London. Series A. **168**, 264 (1938).

[129] B. G. Dick and A. W. Overhauser, *Theory of the Dielectric Constants of Alkali Halide Crystals*, Physical Review **112**, 90 (1958).

[130] J. Tersoff, *New empirical approach for the structure and energy of covalent systems*, Physical Review B **37**, 6991 (1988).

[131] J. Tersoff, *Empirical Interatomic Potential for Carbon, with Applications to Amorphous Carbon*, Physical Review Letters **61**, 2879 (1988).

[132] L. Lindsay and D. A. Broido, *Optimized Tersoff and Brenner empirical potential parameters for lattice dynamics and phonon thermal transport in carbon nanotubes and graphene*, Physical Review B **81**, 205441 (2010).

[133] D. W. Brenner, *Empirical potential for hydrocarbons for use in simulating the chemical vapor deposition of diamond films*, Physical Review B **42**, 9458 (1990).

[134] D. W. Brenner *et al.*, *A second-generation reactive empirical bond order (REBO) potential energy expression for hydrocarbons*, Journal of Physics: Condensed Matter **14**, 783 (2002).

[135] S. J. Stuart, A. B. Tutein, and J. A. Harrison, *A reactive potential for hydrocarbons with intermolecular interactions*, Journal of Chemical Physics **112**, 6472 (2000).

[136] K. Albe, K. Nordlund, and R. S. Averback, *Modeling the metal-semiconductor interaction: Analytical bond-order potential for platinum-carbon*, Physical Review B **65**, 195124 (2002).

[137] N. Juslin *et al.*, *Analytical interatomic potential for modeling nonequilibrium processes in the W-C-H system*, Journal of Applied Physics **98**, 123520 (2005).

[138] Y. Shibuta and S. Maruyama, *Bond-order potential for transition metal carbide cluster for the growth simulation of a single-walled carbon nanotube*, Computational Materials Science **39**, 842 (2007).

[139] K. O. E. Henriksson, C. Björkas, and K. Nordlund, *Atomistic simulations of stainless steels: a many-body potential for the Fe-Cr-C system*, Journal of Physics: Condensed Matter **25**, 445401 (2013).

[140] M. P. Allen and D. J. Tildesley, *Computer Simulation of Liquids* (Oxford University Press, Oxford, 1987).

[141] P. K. Schelling, S. R. Phillpot, and P. Keblinski, *Phonon wave-packet dynamics at semiconductor interfaces by molecular-dynamics simulations*, Applied Physics Letters **80**, 2484 (2002).

[142] P. K. Schelling, S. R. Phillpot, and P. Keblinski, *Kapitza conductance and phonon scattering at grain boundaries by simulation*, Journal of Applied Physics **95**, 6082 (2004).

[143] C. Kimmer, S. Aubry, A. Skye, and P. K. Schelling, *Scattering of phonons from a high-energy grain boundary in silicon: Dependence on angle of incidence*, Physical Review B **75**, 144105 (2007).

[144] W. H. Press, S. A. Teukolsky, W. T. Vetterling, and B. P. Flannery, *Numerical Recipes: The Art of Scientific Computing*, 3:rd ed. (Cambridge University Press, New York, USA, 2007).

[145] G. Kresse and J. Hafner, *Ab initio molecular dynamics for open-shell transition metals*, Physical Review B **48**, 13115 (1993).

[146] G. Kresse and J. Furthmüller, *Efficient iterative schemes for ab initio total-energy calculations using a plane-wave basis set*, Physical Review B **54**, 11169 (1996).

[147] W. Smith, T. R. Forester, and I. T. Todorov, *The DL_POLY_2 user manual* (2009), http://www.cse.scitech.ac.uk/ccg/software /DL_POLY.

[148] S. J. Plimpton, *Fast Parallel Algorithms for Short-Range Molecular Dynamics*, Journal of Computational Physics **117**, 1 (1995), http://lammps.sandia.gov.

[149] S. B. C. Duval *et al.*, *Electrical conductivity of the proton conductor $BaZr_{0.9}Y_{0.1}O_{3-\delta}$ obtained by high-temperature annealing*, Solid State Ionics **178**, 1437 (2007).

[150] T. Tauer, R. O'Hayre, and J. W. Medlin, *Computational investigation of defect segregation at the (001) surface of BaCeO$_3$ and BaZrO$_3$: the role of metal-oxygen bond strenght in controlling vacancy segregation*, Journal of Materials Chemistry A **1**, 2840 (2013).

[151] H.-Y. Cao, H. Xiang, and X.-G. Gong, *Unexpected large thermal rectification in asymmetric grain boundary of graphene*, Solid State Communications **152**, 1807 (2012).

[152] S.-H. Tan *et al.*, *Effect of pentagon-heptagon defect on thermal transport properties in graphene nanoribbons*, Carbon **65**, 181 (2013).

[153] E. E. Helgee and A. Isacsson, http://publications.lib.chalmers.se/records /fulltext/214089/local_214089.pdf (unpublished).

[154] D. H. Chi *et al.*, *Electronic structures of Pt clusters adsorbed on (5,5) single wall carbon nanotube*, Chemical Physics Letters **432**, 213 (2006).

[155] A. Staykov, Y. Ooishi, and T. Ishihara, *Immobilizing Metal Nanoparticles on Single Wall Nanotubes. Effect of Surface Curvature*, Journal of Physical Chemistry C **118**, 8907 (2014).